



Local and regional  
scale measurements  
of CH<sub>4</sub>, δ<sup>13</sup>CH<sub>4</sub>, and  
C<sub>2</sub>H<sub>6</sub> in the Uintah  
Basin

C. W. Rella et al.

Local and regional scale measurements  
of CH<sub>4</sub>, δ<sup>13</sup>CH<sub>4</sub>, and C<sub>2</sub>H<sub>6</sub> in the Uintah  
Basin using a mobile stable isotope  
analyzer

C. W. Rella, J. Hoffnagle, Y. He, and S. Tajima

Picarro, Inc., 3105 Patrick Henry Drive, Santa Clara, CA 95054, USA

Received: 19 February 2015 – Accepted: 25 March 2015 – Published: 13 May 2015

Correspondence to: C. W. Rella (rella@picarro.com)

Published by Copernicus Publications on behalf of the European Geosciences Union.

Title Page

Abstract

Introduction

Conclusions

References

Tables

Figures



Back

Close

Full Screen / Esc

Printer-friendly Version

Interactive Discussion



## Abstract

In this paper, we present an innovative  $\text{CH}_4$ ,  $\delta^{13}\text{CH}_4$ , and  $\text{C}_2\text{H}_6$  instrument based on cavity ring down spectroscopy (CRDS). The design and performance of the analyzer is presented in detail. The instrument is highly precise, capable of precision of less than 1‰ on  $\delta^{13}\text{CH}_4$  with 1 min of averaging and about 0.1‰ in an hour. Using this instrument, we present a comprehensive approach to atmospheric methane emissions attribution. Field measurements were performed in the Uintah Basin (Utah, USA) in the winter of 2013, using a mobile lab equipped with the CRDS analyzer, a high-accuracy GPS, a sonic anemometer, and a novel onboard gas storage and playback system. With a small population and almost no other sources of methane and ethane other than oil and gas extraction activities, the Uintah Basin represents an ideal location to investigate and validate new measurement methods of atmospheric methane and ethane. We present the results of measurements of the individual fugitive emissions from 23 natural gas wells and 6 oil wells in the region. The  $\delta^{13}\text{CH}_4$  and  $\text{C}_2\text{H}_6$  signatures that we observe are consistent with the signatures present in the ground. Furthermore, regional measurements of the atmospheric  $\text{CH}_4$ ,  $\delta^{13}\text{CH}_4$ , and  $\text{C}_2\text{H}_6$  signatures throughout the basin have been made, using continuous sampling into a 450 m long tube. These measurements suggest that  $86 \pm 7\%$  of the total emissions in the basin are from natural gas production.

## 1 Introduction

The advent of the techniques of directional drilling, horizontal drilling, 3-D seismic imaging, and hydraulic fracturing have led to rapid increases in oil and gas production throughout the US, especially in basins where production using so-called conventional methods of extraction were not economically viable. Together with the increase of oil and gas production has been a concurrent increase in gaseous emissions into the atmosphere. Methane, the primary constituent of natural gas, is a potent greenhouse

AMTD

8, 4859–4916, 2015

### Local and regional scale measurements of $\text{CH}_4$ , $\delta^{13}\text{CH}_4$ , and $\text{C}_2\text{H}_6$ in the Uintah Basin

C. W. Rella et al.

Title Page

Abstract

Introduction

Conclusions

References

Tables

Figures

◀

▶

◀

▶

Back

Close

Full Screen / Esc

Printer-friendly Version

Interactive Discussion



## Local and regional scale measurements of CH<sub>4</sub>, δ<sup>13</sup>CH<sub>4</sub>, and C<sub>2</sub>H<sub>6</sub> in the Uintah Basin

C. W. Rella et al.

Title Page

Abstract

Introduction

Conclusions

References

Tables

Figures

◀

▶

◀

▶

Back

Close

Full Screen / Esc

Printer-friendly Version

Interactive Discussion



gas with a global warming potential of 28–86 times that of an equivalent mass of carbon dioxide (Myhre et al., 2013). When emissions are kept under control, methane is a clean burning, high energy content fuel that can reduce carbon dioxide emissions relative to other more carbon-rich fuels. However, when methane emissions are a relatively large fraction of total natural gas production, the climate benefit of methane is reduced or even eliminated (Howarth et al., 2011; Alvarez et al., 2012).

Several recent atmospheric studies using the aircraft mass-balance approach have focused on quantifying regional emissions from oil and gas production. In Pétron et al. (2014), the mass balance approach using aircraft was used to quantify emissions in the Denver–Julesburg basin in Colorado, determining that the methane emissions from fossil fuel extraction activities is about 4 % of total natural gas production in the basin. This emission rate is in excess of both the inventory (Pétron et al., 2012) and the ~ 3 % threshold where there are immediate climate benefits of switching from coal to natural gas electricity production (Alvarez et al., 2012). In the Uintah basin in Utah, again using aircraft, Karion et al. (2013) reported methane emissions (February 2012) to be 6.2–11.7 % of average daily production from the basin, again exceeding the inventory and the threshold for immediate climate benefit. Other studies using this approach are underway in several other basins in the US.

Top-down measurements of regional emissions provide crucial independent verification of bottom-up emission inventories. However, the mass balance measurements of total methane emissions do not provide a means of partitioning the emissions; i.e., determining the relative fraction of emissions contributed by of the source types within the aircraft footprint. While the Uintah basin is fairly simple from the standpoint of methane emissions, with a small population (~ 60 000) and few other sources of methane, the oil and gas producing area in the Denver–Julesburg basin is largely co-located with other sources of methane, such as landfills and concentrated animal feeding operations. Pétron et al. (2014) estimate these emissions to be about 25–30 % of the total on the basis of emission inventories for other sources, such as enteric fermentation, manure management, and solid waste disposal, but without an independent measure-

ment of this inventory, the uncertainty of the emissions attributed to oil and gas activities remains high.

Tracer molecules (i.e., molecules that are co-emitted with methane in different ratios depending upon the emissions sector) can provide valuable information to partition regional emissions. In particular, the stable isotopes of methane and alkanes (ethane, propane, etc.) have been shown to be valuable in partitioning methane emissions between various sources. It has long been understood that low ethane to methane ratios ( $\ll 1\%$ ) and light  $\delta^{13}\text{CH}_4$  signatures below  $-64\text{‰}$  indicate a purely biogenic (i.e., microbial) source (Schoell, 1980), a fact that is exploited in petrochemical exploration to this day. Quay et al. (1988) compiles  $\delta^{13}\text{CH}_4$  signatures from a variety of microbial and abiogenic sources.

The use of the atmospheric signals of  $\delta^{13}\text{CH}_4$  and ethane to infer methane sources and sinks is a relatively new and active area of research. On a global scale, atmospheric measurements of  $\delta^{13}\text{CH}_4$  have been used to partition emissions of methane (Mikaloff-Fletcher et al., 2004a, b). Atmospheric measurements of methane and of  $\delta^{13}\text{CH}_4$  since 1990 have been used to infer changes in the balance between biogenic and thermogenic sources of methane (Kai et al., 2011). Isotopic measurements have also been used to perform source partitioning over time, by analyzing fern air (Bräunlich et al., 2001; Mischler et al., 2009). Ethane has been used in a similar manner globally. For example, Simpson et al. (2012) demonstrated a strong correlation between global ethane concentration and the global methane growth rate to suggest that the overall decrease in the global growth rate of methane over the past 30 years is due to a decrease in oil and gas emissions, although these findings are not fully consistent with other studies (for example, Kirschke et al., 2013) that show tropical wetlands emissions of methane also play an important role. What is clear is that more measurements of these important atmospheric tracers can provide useful constraints on global methane sources and sinks.

These tracers have also been used to infer attribution of emissions on a regional scale.  $\delta^{13}\text{CH}_4$  was used to suggest a relative increase in methane emissions from

## AMTD

8, 4859–4916, 2015

### Local and regional scale measurements of $\text{CH}_4$ , $\delta^{13}\text{CH}_4$ , and $\text{C}_2\text{H}_6$ in the Uintah Basin

C. W. Rella et al.

Title Page

Abstract

Introduction

Conclusions

References

Tables

Figures

◀

▶

◀

▶

Back

Close

Full Screen / Esc

Printer-friendly Version

Interactive Discussion





## Local and regional scale measurements of CH<sub>4</sub>, δ<sup>13</sup>CH<sub>4</sub>, and C<sub>2</sub>H<sub>6</sub> in the Uintah Basin

C. W. Rella et al.

with a four-fold increase in natural gas liquids (UBETS Report, 2013). In addition to the high methane emissions deduced from aircraft measurements (Karion et al., 2013), the Uintah basin suffers from poor air quality due to high production of ozone in the wintertime during atmospheric inversion events. Studies have shown that the gaseous effluents of oil and gas extraction activities in the basin are a key ingredient for the high ozone production (Edwards et al., 2013; Schnell et al., 2012). Although it is clear that the vast majority of methane emissions originate from oil and gas activities (primarily extraction and processing), the relative proportions of emissions associated with the oil production sector and the gas production sector have not been well understood, until now: the mobile CH<sub>4</sub>, δ<sup>13</sup>CH<sub>4</sub>, and C<sub>2</sub>H<sub>6</sub> analysis described in this paper indicates that the emissions from natural gas production comprise 86 ± 7 % (1 – σ) of the emissions in the basin, with the remainder from oil production activities and biogenic sources.

The paper is organized as follows: we first present a detailed description of the CRDS analyzer used in this study, including a thorough discussion of performance, calibration, and cross-interference from other atmospheric constituents. We then describe the mobile laboratory used to perform the measurements, and the methodology employed for characterization of individual sources and regional signals. Results for individual source measurements are presented and compared to studies of the gas composition present in the geologic formations in gas- and oil-producing areas of the basin. These end member populations are then used to interpret the regional atmospheric signal using a simple two end member model. We conclude the paper with a discussion of the findings and present a future outlook for the measurement technology presented.

## 2 Instrument performance

### 2.1 Details of the cavity ring down spectrometer

The methane and ethane measurements were made with an optical analyzer based on cavity ring down spectroscopy (G2132-i, S/N FCDS2016, Picarro, Inc., Santa Clara,

Title Page

Abstract

Introduction

Conclusions

References

Tables

Figures

◀

▶

◀

▶

Back

Close

Full Screen / Esc

Printer-friendly Version

Interactive Discussion



## Local and regional scale measurements of CH<sub>4</sub>, δ<sup>13</sup>CH<sub>4</sub>, and C<sub>2</sub>H<sub>6</sub> in the Uintah Basin

C. W. Rella et al.

Title Page

Abstract

Introduction

Conclusions

References

Tables

Figures

◀

▶

◀

▶

Back

Close

Full Screen / Esc

Printer-friendly Version

Interactive Discussion



CA). CRDS is a laser-based technique in which the infrared absorption loss in a sample cell is measured to quantify the mole-fraction of the gas or gases. Five gas species are measured by these instruments: <sup>12</sup>C<sup>1</sup>H<sub>4</sub>, <sup>13</sup>C<sup>1</sup>H<sub>4</sub>, <sup>1</sup>H<sub>2</sub><sup>16</sup>O, <sup>12</sup>C<sup>2</sup>H<sub>6</sub>, and <sup>12</sup>C<sup>16</sup>O<sub>2</sub> (the latter three denoted H<sub>2</sub>O, C<sub>2</sub>H<sub>6</sub>, and CO<sub>2</sub> from here onward).

Two separate lasers are used in this spectrometer: one for the <sup>12</sup>CH<sub>4</sub> and CO<sub>2</sub> measurements operating at about 6057 wavenumbers, and one for the <sup>13</sup>CH<sub>4</sub>, H<sub>2</sub>O, and C<sub>2</sub>H<sub>6</sub> measurements operating at about 6029 wavenumbers. Light from each laser, tuned to specific near-infrared absorption features of the key analyte molecules, is directed sequentially into an optical resonator (called the optical cavity). The optical cavity consists of a closed chamber with three highly reflective mirrors, and it serves as a compact flow cell with a volume of less than 10 standard cm<sup>3</sup> into which the sample gas is introduced. The sample gas is flowed continuously through the system. The gas flow in the standard instrument is about 25 sccm, but by either modifying the inlet plumbing system and/or restricting the inlet flow, the instrument can be operated at flows from 5–400 sccm. The measurements described in this paper were taken at 400 sccm in the mobile laboratory, for fast response (~ 1 s 10–90 % rise/fall time); and at 15–20 sccm for laboratory work, for conservation of sample gas. The optical cavity is actively controlled to a temperature of 45 °C, and the gas in the cell is actively controlled to a pressure of 148 Torr.

The flow cell has an effective optical path length of 15–20 km; this long path length allows for measurements with high precision (with ppb or even parts-per-trillion uncertainty, depending on the analyte gas), using compact and highly reliable near-infrared laser sources. The gas temperature and pressure are tightly controlled in these instruments (Crosson, 2008). This stability allows the instrument (when properly calibrated to traceable reference standards) to deliver accurate measurements.

The instrument employs precise monitoring and control of the optical wavelength, which delivers sub-picometer wavelength targeting on a microsecond timescale. Ring down events are collected at a rate of about 200 ringdowns s<sup>-1</sup>. Individual spectrograms consist of about 50–200 individual ring downs, distributed across 10–20 spectral

## Local and regional scale measurements of CH<sub>4</sub>, δ<sup>13</sup>CH<sub>4</sub>, and C<sub>2</sub>H<sub>6</sub> in the Uintah Basin

C. W. Rella et al.

Title Page

Abstract

Introduction

Conclusions

References

Tables

Figures

◀

▶

◀

▶

Back

Close

Full Screen / Esc

Printer-friendly Version

Interactive Discussion



points around the peak. The overall measurement interval is about 1 s. The resulting spectrograms are analyzed using nonlinear spectral pattern recognition routines, and the outputs of these routines are converted into gas concentrations using linear conversion factors derived from calibration activities using gas standards that are traceable to gravimetric standards or other artifact standards, as described below.

### 2.2 <sup>12</sup>CH<sub>4</sub> and <sup>13</sup>CH<sub>4</sub> spectroscopy

The right panel of Fig. 1 displays the spectra of key gas species (the analytes and other key atmospheric constituents) in the 6057 wavenumber region, generated with the HITRAN database (Rothman et al., 2013) for CH<sub>4</sub>, CO<sub>2</sub>, and H<sub>2</sub>O. The spectral feature used for quantification of <sup>12</sup>CH<sub>4</sub> is a quartet of lines centered at about 6057.07 wavenumbers. The laser is scanned across this spectral feature, from about 6056.81 to 6057.39 with approximately 0.02 wavenumber resolution. The resulting spectrograms are fit with a modified nonlinear Levenberg–Marquardt (Press et al., 1986) algorithm, using an experimentally derived model function for <sup>12</sup>CH<sub>4</sub>. Due to the complexity of the spectrum, instead of modeling the observed spectrum with an ensemble of single ro-vibrational transitions, we have constructed an empirically-derived model based on a cubic spline with knots spaced approximately every 0.01 wavenumbers.

We note that the spectral region and the analysis algorithms for <sup>12</sup>CH<sub>4</sub> is identical to the algorithms that are used in several standard models from the same manufacturer (e.g., models G1301, G2301, G2401); the performance of these instruments for atmospheric measurements of CH<sub>4</sub>, and H<sub>2</sub>O has been described in detail elsewhere (Crosson, 2008; Chen et al., 2010; Rella et al., 2013; Fang et al., 2013; Winderlich et al., 2010). The basic performance reported in these papers should be highly representative of the performance of this analyzer, and we will rely on these references for estimates of precision, uncertainty, and cross-talk with key analytical species.

The left panel of Fig. 1 displays the spectra of key gas species (the analytes and other key atmospheric constituents) in the 6029 wavenumber region. The individual spectra were generated from the HITRAN database (Rothman et al., 2013) for CH<sub>4</sub>, CO<sub>2</sub>, and



**Local and regional scale measurements of CH<sub>4</sub>, δ<sup>13</sup>CH<sub>4</sub>, and C<sub>2</sub>H<sub>6</sub> in the Uintah Basin**

C. W. Rella et al.

Title Page

Abstract

Introduction

Conclusions

References

Tables

Figures

◀

▶

◀

▶

Back

Close

Full Screen / Esc

Printer-friendly Version

Interactive Discussion

H<sub>2</sub>O, and from experimental measurements for ethane, which is not included in the database. During normal instrument operation, the region of 6028.4–6029.2 wavenumbers is scanned with approximately 0.02 wavenumber resolution. The resulting spectrograms are fit, using experimentally determined model functions for <sup>12</sup>CH<sub>4</sub>, <sup>13</sup>CH<sub>4</sub>, H<sub>2</sub>O, and CO<sub>2</sub>. The latter two spectra are quite simple, and were modeled with Galatry functions.

The <sup>12</sup>CH<sub>4</sub> and <sup>13</sup>CH<sub>4</sub> are more complicated to model. In an experimental instrument, fine scan spectra over a range of 6028.4 to 6029.2 wavenumbers were collected on a sample of 100 ppm CH<sub>4</sub> and δ<sup>13</sup>CH<sub>4</sub> ~ -40‰ in a balance of synthetic air. A separate sample of > 99% pure <sup>13</sup>CH<sub>4</sub> was used to verify that only the three lines at 6029.1 are the only significant <sup>13</sup>CH<sub>4</sub> features in this region. All the other lines (about two dozen distinct features, according to the more recent HITRAN database, which was not available in 2010 when the initial spectroscopic work was performed) are due to <sup>12</sup>CH<sub>4</sub>. The <sup>13</sup>CH<sub>4</sub> triplet is modeled with Galatry functions (Varghese and Hanson, 1984). The contribution of the <sup>13</sup>CH<sub>4</sub> lines were subtracted from the experimental composite CH<sub>4</sub> spectrum, in principle leaving only <sup>12</sup>CH<sub>4</sub>. The <sup>12</sup>CH<sub>4</sub> spectrum was then modeled from this processed spectrum, using a combination of three Galatry functions for the prominent <sup>12</sup>CH<sub>4</sub> peaks and a cubic spline with knots spaced approximately every 0.01 wavenumbers for the smaller peaks. It is possible that in this process that either “too much” or “too little” <sup>13</sup>CH<sub>4</sub> was removed from the composite spectrum. This would lead to a cross-interference between <sup>12</sup>CH<sub>4</sub> and <sup>13</sup>CH<sub>4</sub>, which can be dealt with in a straightforward manner during the calibration of δ<sup>13</sup>CH<sub>4</sub>, as discussed below.

The amplitudes of the <sup>12</sup>CH<sub>4</sub>, <sup>13</sup>CH<sub>4</sub>, and H<sub>2</sub>O spectral features are varied dynamically in the nonlinear fit routine to minimize the least squares. The amplitude of the CO<sub>2</sub> is determined from a quasi-simultaneous measurement of CO<sub>2</sub> made at 6056.51 wavenumbers. CO<sub>2</sub> is measured by scanning from 6056.4 to 6056.6 wavenumbers, across the <sup>12</sup>CO<sub>2</sub> spectral feature. This measurement is only a rough measurement by

atmospheric standards ( $\sim 1$  ppm uncertainty), but it is sufficient for the purpose of presetting the amplitude of the  $\text{CO}_2$  lines in the vicinity of the  $^{13}\text{CH}_4$  feature.

From this nonlinear fit, the water concentration is also determined using the peak height of the water feature centered at 6028.79 wavenumbers. In addition, a second independent nonlinear fit is performed in which the model function of  $\text{C}_2\text{H}_6$  is also included in the fit, which allows us to quantify the ethane concentration in a gas sample with approximately 100 ppb precision. This relatively poor precision, coupled with an uncorrected cross-interference with some key gas species, limits the general utility of this measurement. The performance and limitations of this measurement are discussed below.

There are two modes of operation in this instrument. In one mode, called the “high precision” mode, the  $^{12}\text{CH}_4$  is quantified using the very strong feature at about 6057.07 wavenumbers. In the second mode, called the “high range” mode, the  $^{12}\text{CH}_4$  is quantified using the weaker feature at 6028.55 wavenumbers. This line has a much stronger dynamic range, above 1000 ppm  $\text{CH}_4$ . In this paper, we consider only the “high-precision” mode of the analyzer. In addition, we will devote most of our attention to the performance of  $^{12}\text{CH}_4$  and  $^{13}\text{CH}_4$  (and thus  $\delta^{13}\text{CH}_4$ ), since these are the primary analyte gas species. We will also discuss the calibration and uncertainty in the  $\text{H}_2\text{O}$ ,  $\text{CO}_2$ , and  $\text{C}_2\text{H}_6$  measurements, especially in the context of using these measurements to correct for cross-interference of these species onto the primary analyte gases.

### 2.3 Precision and Allan standard deviation

We have performed a basic assessment of the instrument by measuring a single bottle (1.78 ppm  $\text{CH}_4$ ) for 18 h. We have computed the Allan standard deviation (Allan, 1966) of the resulting data set, using the following definition:

$$\sigma^2(\tau) = \frac{1}{2N} \sum_{i=1}^N [y(\tau)_{i+1} - y(\tau)_i]^2 \quad (1)$$

## Local and regional scale measurements of $\text{CH}_4$ , $\delta^{13}\text{CH}_4$ , and $\text{C}_2\text{H}_6$ in the Uintah Basin

C. W. Rella et al.

Title Page

Abstract

Introduction

Conclusions

References

Tables

Figures

◀

▶

◀

▶

Back

Close

Full Screen / Esc

Printer-friendly Version

Interactive Discussion



## Local and regional scale measurements of CH<sub>4</sub>, δ<sup>13</sup>CH<sub>4</sub>, and C<sub>2</sub>H<sub>6</sub> in the Uintah Basin

C. W. Rella et al.

Title Page

Abstract

Introduction

Conclusions

References

Tables

Figures

◀

▶

◀

▶

Back

Close

Full Screen / Esc

Printer-friendly Version

Interactive Discussion



In this expression,  $y(\tau)_i$  are sequential block averages over time  $\tau$ . The Allan standard deviations for  $\delta^{13}\text{CH}_4$ ,  $\text{CH}_4$ , and  $\text{C}_2\text{H}_6$  are shown in Fig. 2. The noise isotope ratio and ethane at 1 min of averaging is below 1.0‰ and 25 ppb, respectively, and continue to follow a square root averaging law to about an hour or more. This high degree of stability can be used to conduct highly accurate experiments, especially when calibration gases are introduced periodically, as will be seen below.

## 2.4 Calibration

### 2.4.1 <sup>12</sup>CH<sub>4</sub>

The spectroscopic line used to quantify <sup>12</sup>CH<sub>4</sub> is the same as that used in several widely-deployed instruments produced by the same manufacturer (e.g., Models G2301 and G2401). The spectroscopy and analysis codes are identical, apart from two small differences:

1. The operating pressure differs by 8 Torr; i.e., 148 Torr in this instrument vs. 140 Torr in the other models.
2. The absorption line used to quantify water vapor is different between this model and the other instrumentation.

These two differences lead to small differences in the <sup>12</sup>CH<sub>4</sub> calibration factors and the coefficients used to report and correct for water vapor in the gas stream. These effects are investigated below.

The output of the spectroscopic fitting algorithm is a peak height corresponding to the analyte gas. The function relating the mole fraction  $c$  to the absorption peak area is linear, according to the Beer–Lambert law. The peak height  $\alpha$  is not always a linear relationship, but in most situations in near-infrared resolved ro-vibrational optical spectroscopy, this expression is substantially linear:

$$c_{12} = k_{12}\alpha_{12} + \varepsilon_{12} \quad (2)$$

## Local and regional scale measurements of CH<sub>4</sub>, δ<sup>13</sup>CH<sub>4</sub>, and C<sub>2</sub>H<sub>6</sub> in the Uintah Basin

C. W. Rella et al.

Title Page

Abstract

Introduction

Conclusions

References

Tables

Figures

◀

▶

◀

▶

Back

Close

Full Screen / Esc

Printer-friendly Version

Interactive Discussion



The constant of proportionality  $k_{12}$  relates the measured absorption peak height  $\alpha_{12}$  to the mole fraction of  $^{12}\text{CH}_4$  in the sample gas  $c_{12}$ , with an offset term  $\varepsilon_{12}$ . In the absence of other background gas effects (a topic discussed fully below),  $k_{12}$  is a constant  $\kappa_{12}$  that is equal to  $4.333 \text{ ppb}^{12}\text{CH}_4$  per  $\text{ppb cm}^{-1}$  of loss<sup>1</sup>, determined by performing a measurement of a calibrated tank with a single instrument (Model G2132-i, serial number FCDS2016, Picarro, Inc., Santa Clara, USA). The analytical accuracy of this tank is 1%, which is more than sufficient for this study. For more demanding applications, the instrument can be calibrated using standard gas mixtures with lower uncertainty, which also allows one to determine the offset term  $\varepsilon_{12}$ , which is typically within a few ppb of zero.

### 2.4.2 $\delta^{13}\text{CH}_4$

The  $^{13}\text{CH}_4$  concentration is determined from the measured absorption peak height, using a similar treatment as for  $^{12}\text{CH}_4$ . We begin with the simple linear relationship:

$$c_{13} = k_{13}\alpha_{13} + \varepsilon_{13} \quad (3)$$

In principle, with careful measurements, we could determine calibration constants for  $^{13}\text{CH}_4$  as was done for  $^{12}\text{CH}_4$ . However, we have chosen a strategy of selecting  $\delta^{13}\text{CH}_4$  as the primary isotopic measurement output, rather than  $^{13}\text{CH}_4$ , for the following reasons:

1. It is experimentally more straightforward to generate a constant  $\delta^{13}\text{CH}_4$  in a varying background gas mixture than it is to generate a constant  $^{13}\text{CH}_4$  mixture.
2. Dilution by water vapor occurs to both species equally (as a % of each species' dry mole fraction), which means that  $\delta^{13}\text{CH}_4$  is unaffected by dilution.

<sup>1</sup>ppb $\text{cm}^{-1}$ , or parts-per-billion per cm, is a unit that describes optical absorbance per distance.

## Local and regional scale measurements of CH<sub>4</sub>, δ<sup>13</sup>CH<sub>4</sub>, and C<sub>2</sub>H<sub>6</sub> in the Uintah Basin

C. W. Rella et al.

Title Page

Abstract

Introduction

Conclusions

References

Tables

Figures

◀

▶

◀

▶

Back

Close

Full Screen / Esc

Printer-friendly Version

Interactive Discussion



3. Spectral line shape effects are likely to have similar effects on the two species. δ<sup>13</sup>CH<sub>4</sub> is affected only by the *net* line shape effect between the two species.
4. δ<sup>13</sup>C is commonly reported on the Vienna Pee Dee Belemnite scale (Coplen et al., 2006), for which there are traceable primary standards. In contrast, there are no independent primary standards for <sup>13</sup>CH<sub>4</sub>; the scale for <sup>13</sup>CH<sub>4</sub> is typically defined by a combination of the δ<sup>13</sup>CH<sub>4</sub> standard and the total CH<sub>4</sub> scale.

Throughout this paper, we will consider <sup>12</sup>CH<sub>4</sub> and δ<sup>13</sup>CH<sub>4</sub> as the independently calibrated quantities. The individual concentration <sup>13</sup>CH<sub>4</sub> will be derived directly from these two analytical values using the following expression:

$$\delta^{13}\text{CH}_4[\text{in}\text{‰}] \equiv 1000 \left( \frac{r_{\text{sample}}}{r_{\text{VPDB}}} - 1 \right), \text{ where } r_{\text{sample}} = c_{13}/c_{12} \text{ and } r_{\text{VPDB}} = 0.0111802 \quad (4)$$

The value for  $r_{\text{VPDB}}$  follows Werner and Brand (2001). Substituting the simple linear relationships for  $c_{12}$  and  $c_{13}$  (Eqs. 2 and 3) into this expression, we find

$$\delta^{13}\text{CH}_4 = 1000 \left( \frac{k_{13}\alpha_{13} + \varepsilon_{13}}{(k_{12}\alpha_{12} + \varepsilon_{12})r_{\text{VPDB}}} - 1 \right) \quad (5)$$

Equation (5) relates the spectroscopic measurements of absorption loss at the peak of the two isotopologues ( $\alpha_{12}$  and  $\alpha_{13}$ ), the calibration coefficients ( $k_{12}$  and  $k_{13}$ ), and the calibration offsets ( $\varepsilon_{12}$  and  $\varepsilon_{13}$ ) to the determination of δ<sup>13</sup>CH<sub>4</sub>.

First, we consider the case of an ideal spectrometer, for which the calibration coefficients are constants (i.e.,  $k_{12} = \kappa_{12}$  and  $k_{13} = \kappa_{13}$ ), and the calibration offsets are zero (i.e.,  $\varepsilon_{12} = \varepsilon_{13} = 0$ ). These assumptions lead to the following expression, as expected:

$$\delta^{13}\text{CH}_4 = 1000 \left[ \frac{\left( \frac{\kappa_{13}\alpha_{13}}{\kappa_{12}\alpha_{12}} \right)}{r_{\text{VPDB}}} - 1 \right] \quad (6)$$

## Local and regional scale measurements of CH<sub>4</sub>, δ<sup>13</sup>CH<sub>4</sub>, and C<sub>2</sub>H<sub>6</sub> in the Uintah Basin

C. W. Rella et al.

Equation (6) can be used to calibrate the instrument, as it relates the spectroscopically measurable quantities (i.e., the loss ratio  $\frac{\alpha_{13}}{\alpha_{12}}$ ) to  $\delta^{13}\text{CH}_4$ . The factory calibration for this set of spectroscopic lines was obtained using the following method. A single bottle of 100 ppm methane (Air Liquide America Specialty Gases, Plumsteadville, Pennsylvania, USA) was used as a source gas. Several one liter sampling bags (Cali-5-Bond, Calibrated Instruments, Hawthorne, NY, USA) were filled with the source gas. The bags were equipped with a silicone septum mounted directly on the bag. Pure  $^{12}\text{CH}_4$  (model, vendor) was injected through the septum in varying amounts to each bag to shift the isotope ratio in the samples. These bags were then measured on an instrument (serial number FCDS002) after diluting 10 : 1 with methane-free zero air, and then these bags were subsequently sent for analysis at commercial laboratory (Isotech, Champaign, Illinois, USA). Figure 3 shows these calibration data. The samples cover a relatively narrow range of delta, from  $-60$  to  $-67$ ‰. By fitting the data to a line of the form

$$\left[\delta^{13}\text{CH}_4\right]_{\text{standard}} = A \frac{\alpha_{13}}{\alpha_{12}} + B \quad (7)$$

we obtain  $A = 165\,595.70$ ‰ and  $B = -1053.59$ ‰. These calibration constants have been transferred to all subsequent instruments.

To validate the calibration over a wider range of delta, we used four isotope standards at a concentration of 2500 ppm CH<sub>4</sub> in a balance of air (Isometric Instruments, Victoria, British Columbia, Canada), with isotope ratios ranging from  $-66.5$  to  $-23.9$ ‰, and an uncertainty of  $\pm 0.2$ ‰ (as quoted by the supplier). These standards were diluted with zero air using the setup shown in Fig. 4. For each isotope standard, four concentration steps were generated by changing the flow in the mass flow controller, with the output concentration ranging from 2–20 ppm. The values reported by the instrument were generated using the standard instrument calibration constants. The top panel of Fig. 5 shows the resulting data, along with a linear fit (green line) and the standard calibration (red dashed line). The new instrument calibration is given by the constants

$$A' = 153\,947$$
‰ and  $B' = -983.29$ ‰. (8)

[Title Page](#)
[Abstract](#)
[Introduction](#)
[Conclusions](#)
[References](#)
[Tables](#)
[Figures](#)
[◀](#)
[▶](#)
[◀](#)
[▶](#)
[Back](#)
[Close](#)
[Full Screen / Esc](#)
[Printer-friendly Version](#)
[Interactive Discussion](#)


## Local and regional scale measurements of CH<sub>4</sub>, δ<sup>13</sup>CH<sub>4</sub>, and C<sub>2</sub>H<sub>6</sub> in the Uintah Basin

C. W. Rella et al.

Title Page

Abstract

Introduction

Conclusions

References

Tables

Figures

◀

▶

◀

▶

Back

Close

Full Screen / Esc

Printer-friendly Version

Interactive Discussion



This calibration has a 7% difference in slope from the initial calibration. The bottom panel shows the residuals of the linear fit (green circles), as well as the difference between the original calibration and the standard values (red values). The two calibration functions give results that are in reasonably good agreement in the –55 to –35% range. Given the much wider range of these calibration standards, this later calibration is likely to be more accurate in the high and low delta ranges. Results in this paper are reported against the scale defined by these four standards.

Note that it is recommended that each instrument of this model be calibrated separately and independently, over the relevant range of delta that will be encountered in the experiment, and with sufficient frequency in time (daily or even more frequently) to track any drift in the analyzer. This topic will be discussed in greater detail below.

The calibration slope parameter  $A'$  can be used to infer the peak height ratio  $\frac{\kappa_{13}}{\kappa_{12}}$  from the expression  $A' = \frac{1000 \left( \frac{\kappa_{13}}{\kappa_{12}} \right)}{r_{\text{VPDB}}}$ , obtained from inspection of Eqs. (6) and (7). Given  $r_{\text{VPDB}} = 0.0111802$ , we find that  $\frac{\kappa_{13}}{\kappa_{12}} = 1.7212$  which means that  $\kappa_{13} = 7.458 \text{ ppb}^{13}\text{CH}_4$  per ppb  $\text{cm}^{-1}$  of loss. For  $\delta^{13}\text{CH}_4 = 0.0 \text{ ‰}$ , the  $^{13}\text{CH}_4$  line is 154 times smaller than the  $^{12}\text{CH}_4$  line.

### 2.5 Instrument drift and methods for correction

To design an effective calibration and drift correction routine, it is important to understand how the optical spectrometer drifts, and how best to correct for that drift. In Section A of the Supplement, we present in detail the nonlinearity of the instrument as a function of methane concentration. We begin by inspecting Eq. (S5) in the Supplement, reproduced below (where we have not included the nonlinear term  $\gamma$ ):

$$\left\{ \delta^{13}\text{CH}_4 \right\}_{\text{spectr. corr}} = \frac{1000}{r_{\text{VPDB}}} \left[ \frac{k_{13}\alpha_{13}}{k_{12}\alpha_{12}} + \frac{\alpha_0}{\alpha_{12}} \right] + \left( \frac{1000}{r_{\text{VPDB}}} \frac{k_{13}}{k_{12}} \beta - 1000 \right) \quad (9)$$

## Local and regional scale measurements of CH<sub>4</sub>, δ<sup>13</sup>CH<sub>4</sub>, and C<sub>2</sub>H<sub>6</sub> in the Uintah Basin

C. W. Rella et al.

Title Page

Abstract

Introduction

Conclusions

References

Tables

Figures

◀

▶

◀

▶

Back

Close

Full Screen / Esc

Printer-friendly Version

Interactive Discussion



As has been discussed in the Supplement, the net loss offset term  $\alpha_0$  is due to imperfections in the spectrometer response. There is no reason to assume that these imperfections are constant in time – we therefore include an explicit dependence of this term on time, or  $\alpha_0(t)$ . There are also spectrometer drifts and errors that can affect the calibration coefficients  $k_{12}$  and  $k_{13}$ . Examples of this type of drift are cavity temperature or pressure drifts, where the changes are manifest in the absorption cross-sections and line shapes. Drifts in the wavelength axis also tend to be proportional to the absorption peak height, and therefore affect  $k_{12}$  and  $k_{13}$ . We will assume that the drift in the ratio of the slope coefficients takes on the form  $\frac{k_{13}}{k_{12}} = (1 + \chi(t))\frac{k_{13}}{k_{12}}$ , where  $\chi(t)$  is small. Finally, the term  $\beta$  quantifies the degree to which the <sup>13</sup>CH<sub>4</sub> loss measurement  $\alpha_{13}$  is dependent of the concentration of <sup>12</sup>CH<sub>4</sub> ( $\alpha_{13}$  is independent of <sup>12</sup>CH<sub>4</sub> when  $\beta = 0$ ). To capture potential drift in this term, we will include an explicit dependence of the term  $\beta$  on time:  $\beta(t) = \beta_0(1 + b(t))$ . We do not expect the physical processes that lead to a non-zero  $\beta$  (i.e., nonlinearity in the absorbance axis and cross-talk between <sup>12</sup>CH<sub>4</sub> and <sup>13</sup>CH<sub>4</sub>) to drift significantly over time compared to the other two terms, but we include it for completeness. Keeping terms to first order in  $\chi(t)$  and  $b(t)$ , we find:

$$\left[ \delta^{13}\text{CH}_4 \right]_{\text{true}} = 1000 \left[ \frac{\left( \frac{k_{13}\alpha_{13}}{k_{12}\alpha_{12}} \right) + \chi(t) \left( \frac{k_{13}\alpha_{13}}{k_{12}\alpha_{12}} \right) + \frac{\alpha_0(t)}{\alpha_{12}}}{r_{\text{VPDB}}} \right] + \left( \frac{1000}{r_{\text{VPDB}}} \frac{k_{13}}{k_{12}} \beta_0 - 1000 \right) + \frac{1000}{r_{\text{VPDB}}} \frac{k_{13}}{k_{12}} \beta_0 (\chi(t) + b(t)) \quad (10)$$

If we substitute in this equation the calibration terms  $A'$  and  $B'$  and regroup, we arrive at the following expression:

$$\left[ \delta^{13}\text{CH}_4 \right]_{\text{true}} = A' \frac{\alpha_{13}}{\alpha_{12}} + B' + \frac{c_0(t)}{c_{12}} + \chi(t) A' \frac{\alpha_{13}}{\alpha_{12}} + C'(t) \quad (11)$$



## Local and regional scale measurements of CH<sub>4</sub>, δ<sup>13</sup>CH<sub>4</sub>, and C<sub>2</sub>H<sub>6</sub> in the Uintah Basin

C. W. Rella et al.

$$\text{Where } A' = \frac{1000 \left( \frac{\kappa_{13}}{\kappa_{12}} \right)}{r_{\text{VPDB}}}$$

$$B' = \left( \frac{1000}{r_{\text{VPDB}}} \frac{\kappa_{13}}{\kappa_{12}} \beta_0 - 1000 \right) = A' \beta_0 - 1000,$$

$$C'(t) = A' \beta_0 (\chi(t) + b(t)).$$

5 Noting that  $A' \frac{\alpha_{13}}{\alpha_{12}} + B' = [\delta^{13}\text{CH}_4]_{\text{raw}}$ , this simplifies to:

$$[\delta^{13}\text{CH}_4]_{\text{true}} = [\delta^{13}\text{CH}_4]_{\text{raw}} + \frac{c_0(t)}{c_{12}} + \chi(t) \left( [\delta^{13}\text{CH}_4]_{\text{raw}} - B' \right) + C'(t) \quad (12)$$

Equation (12) shows that as the spectrometer drifts, changes in  $c_0(t)$ ,  $\chi(t)$ , and  $C'(t)$  manifest as three drift terms: one term that is proportional to  $[\delta^{13}\text{CH}_4]_{\text{raw}} - B'$  (a term which is approximately proportional to the ratio of the loss ratio  $\frac{\alpha_{13}}{\alpha_{12}}$ , as can be seen from Eq. (7), and thus the ratio  $c_{13}/c_{12}$ ); one term that is inversely proportional to the methane concentration  $c_{12}$ , and a simple offset term  $C'(t)$  that depends on neither concentration nor delta. This result is analogous to a similar expression derived in Griffith et al. (2012) for measurements of  $\delta^{13}\text{CO}_2$  using a Fourier Transform Infrared Spectrometer, indicating the general applicability of the mathematical approach to isotope ratio measurements based on infrared spectroscopy. We recall that variability the terms  $c_0(t)$ ,  $\chi(t)$ , and  $C'(t)$  are driven by different physical processes (i.e., spectral variations in the optical loss of the empty cavity; errors in the temperature or pressure of the gas, or changes in the wavelength calibration; and changes in the cross-talk between the two methane isotopologues, respectively). We take advantage of these differences to devise a method of drift correction in the next section.

Title Page

Abstract

Introduction

Conclusions

References

Tables

Figures

◀

▶

◀

▶

Back

Close

Full Screen / Esc

Printer-friendly Version

Interactive Discussion



## 2.5.1 Two bottle drift correction testing

For this experiment, we will assume that the term  $C'(t)$  is zero. The two remaining drift terms  $c_0(t)$  and  $\chi(t)$  have a markedly different dependence on concentration. Therefore, to effectively track drift, we will use two bottles with different  $\text{CH}_4$  concentrations.

Note that to track the term  $C'(t)$ , it would be necessary to introduce a third bottle with a substantially different isotope ratio than at least one of the first two bottles. Although the algebra becomes more complicated, the outcome is similar to calibration using two bottles.

We conducted an experiment with two bottles (Fig. 6): a high concentration bottle (HI) of about 10 ppm  $\text{CH}_4$  and  $\delta^{13}\text{CH}_4 = -41.7\text{‰}$  and a low concentration bottle (LO) of about 1.8 ppm and  $\delta^{13}\text{CH}_4 = -44.5\text{‰}$ . A third unknown bottle at about 2 ppm was used as a target tank to quantify the performance of the system. During each hour, 10 min were spent measuring the HI tank, 25 min for the LO tank, and 25 min for the Target tank. This cycle was repeated every hour for forty days using a single instrument and a single set of tanks.

Figure 7 shows the isotope ratios measured by the instrument for each of the three bottles over time. Clearly, there is significant drift in the instrument. The lower concentration bottles drift much more than the high concentration (about 5 vs. 1 ‰), indicating that  $c_0(t)$  is the dominant source of drift in these data.

For each cylinder (HI and LO) measurement during each hour, we may derive an equation based on Eq. (12) that describes the terms  $\chi(t_i)$  and  $c_0(t_i)$ :

$$\begin{aligned}\delta_{\text{HI}} &= \delta_{\text{H}}(t_i) + \chi(t_i)(\delta_{\text{H}}(t_i) - B) + \frac{c_0(t_i)}{c_{12\text{H}}} \\ \delta_{\text{LO}} &= \delta_{\text{L}}(t_i) + \chi(t_i)(\delta_{\text{L}}(t_i) - B) + \frac{c_0(t_i)}{c_{12\text{L}}}\end{aligned}\quad (13)$$

### Local and regional scale measurements of $\text{CH}_4$ , $\delta^{13}\text{CH}_4$ , and $\text{C}_2\text{H}_6$ in the Uintah Basin

C. W. Rella et al.

Title Page

Abstract

Introduction

Conclusions

References

Tables

Figures

◀

▶

◀

▶

Back

Close

Full Screen / Esc

Printer-friendly Version

Interactive Discussion



In the above expressions,  $\delta_L(t_i) \equiv [\delta^{13}\text{CH}_4]_{\text{raw-LO}}(t_i)$  and  $\delta_H(t_i) \equiv [\delta^{13}\text{CH}_4]_{\text{raw-HI}}(t_i)$ , and  $\delta_{\text{HI,LO}}$  are the isotope assignments for each tank.

In addition, we define:

$$\Delta_H \equiv \delta_{\text{HI}} - \delta_H(t_i) \text{ and } \Delta_L \equiv \delta_{\text{LO}} - \delta_L(t_i) \quad (14)$$

Using these definitions and Eq. (13), we can derive the time dependent drift parameters  $\chi(t_i)$  and  $c_0(t_i)$ :

$$c_0(t_i) = \frac{[\Delta_H(\delta_L(t_i) - B) - \Delta_L(\delta_H(t_i) - B)]}{\left[ \frac{(\delta_L(t_i) - B)}{c_{12\text{H}}} - \frac{(\delta_H(t_i) - B)}{c_{12\text{L}}} \right]}$$

$$\chi(t_i) = \frac{\left[ \Delta_H - \frac{c_0(t_i)}{c_{12\text{H}}} \right]}{(\delta_H(t_i) - B)} \quad (15)$$

In other words, for each hour, we can determine the calibration factors  $\chi(t_i)$  and  $\alpha_0(t_i)$  from isotope and  $^{12}\text{CH}_4$  loss measurements of each tank. Figure 8 displays these calibration factors determined from each hourly cycle over the forty day duration of the experiment. The primary source of drift is the term  $c_0(t_i)$ , although  $\chi(t_i)$  also drifts to a small extent.

Using these calibration constants, we can calculate  $[\delta^{13}\text{CH}_4]_{\text{true}}$  on an hourly basis, using Eq. (12), which is shown in Fig. 9, along with the 24 h average of these data, with SD of  $\pm 0.21$  and  $\pm 0.05\text{‰}$ , respectively. This stability is comparable to the measurement stability of  $\delta^{13}\text{CH}_4$  achieved by a high-quality isotope laboratory (Lowe et al., 2002). We have calculated the Allan standard deviation of the data (Fig. 10). The Allan standard deviation follows a  $\tau^{-1/2}$  law past 100 h of averaging, indicating that the instrument calibrated in this manner is stable over long periods of time. This high degree of stability strongly supports the possibility that this instrument can be used for long-term in situ atmospheric monitoring of  $\delta^{13}\text{CH}_4$ .

**Local and regional scale measurements of  $\text{CH}_4$ ,  $\delta^{13}\text{CH}_4$ , and  $\text{C}_2\text{H}_6$  in the Uintah Basin**

C. W. Rella et al.

Title Page

Abstract

Introduction

Conclusions

References

Tables

Figures

◀

▶

◀

▶

Back

Close

Full Screen / Esc

Printer-friendly Version

Interactive Discussion



## 2.6 Cross-interference from other species

It is clearly important that for the instrument to be of practical use, it must precisely and accurately report the analyte mole fractions ( $^{12}\text{CH}_4$  and  $\delta^{13}\text{CH}_4$ ) over a wide range of variability in the background gas matrix, especially including species such as  $\text{H}_2\text{O}$  and  $\text{CO}_2$ , which are known to vary significantly in practical field situations. As is clear from Fig. 1, the near-infrared spectra of the key analyte species are not free of spectral interference from other ro-vibrational absorption lines due to these gas species and other atmospheric constituents. In an ideal spectrometer, using ideal model functions that perfectly describe the absorption spectrum of the gas mixture present in the flow cell, the analysis of the spectra will in principle reproduce the mole fractions of the analyte gas without loss of fidelity. In the real world, however, there are practical limitations to the quality of the spectroscopic model underlying the measurements, which leads to unwanted biases in the reported analyte concentrations as the background gas matrix varies. We call these biases cross-interferences. In the Supplement, Sect. A, we present in detail the cross interferences on  $^{12}\text{CH}_4$  and  $\delta^{13}\text{CH}_4$  by a variety of atmospheric constituents. The results of this work are summarized in the Table 1. We discuss each species from the table below.

- *Oxygen and Argon*: these two gas species do not have any direct spectroscopic absorption in the spectral regions used in the analyzer to quantify methane. They affect the reported methane as a shift in the reported isotope ratio that is proportional to the concentration of the gas. This shift is independent of the methane concentration. Note that the balance gas is nitrogen in these experiments.
- *Water vapor and carbon dioxide*: these two gas species have direct absorption features that are in the vicinity of the  $^{12}\text{CH}_4$  and  $^{13}\text{CH}_4$  absorption lines; these features are incorporated in the spectral models that are used to fit the measured absorption spectra. To the extent that the models are perfect, there would be no cross-interference with  $\delta^{13}\text{CH}_4$ . Experimentally, we find that there are some small deviations in  $\delta^{13}\text{CH}_4$ , especially due to water (these experiments are discussed in

### Local and regional scale measurements of $\text{CH}_4$ , $\delta^{13}\text{CH}_4$ , and $\text{C}_2\text{H}_6$ in the Uintah Basin

C. W. Rella et al.

Title Page

Abstract

Introduction

Conclusions

References

Tables

Figures

◀

▶

◀

▶

Back

Close

Full Screen / Esc

Printer-friendly Version

Interactive Discussion



## Local and regional scale measurements of CH<sub>4</sub>, δ<sup>13</sup>CH<sub>4</sub>, and C<sub>2</sub>H<sub>6</sub> in the Uintah Basin

C. W. Rella et al.

Title Page

Abstract

Introduction

Conclusions

References

Tables

Figures

◀

▶

◀

▶

Back

Close

Full Screen / Esc

Printer-friendly Version

Interactive Discussion



greater detail in the Supplement). These effects are nonlinear. We provide a range of values that captures 95 % of the measurements under varying contaminant gas conditions as described in the far right column of the table. For the most accurate results, it is recommended that the gas stream be dried to < 0.1 % mole fraction of water vapor prior to analysis, and that the variability of carbon dioxide be limited if possible.

- *Ethane, ammonia, hydrogen sulfide, methyl mercaptan, propane, butane, ethylene*: we have investigated the effect of these gases on the measurement of δ<sup>13</sup>CH<sub>4</sub>. The primary effect that these gases have is to distort the measured absorption spectrum, which in turn leads to an error in the measurement of δ<sup>13</sup>CH<sub>4</sub>. The magnitude of this effect is proportional to the mole fraction of the contaminant species, and inversely proportional to the methane concentration (because at higher methane concentrations, a given distortion of the spectrum has a smaller effect on the isotope ratio). For example, 0.3 ppm of ethane in a gas stream of 3 ppm of CH<sub>4</sub> would shift the δ<sup>13</sup>CH<sub>4</sub> measurement higher by  $[+35\% \text{ ppm CH}_4 (\text{ppm C}_2\text{H}_6)^{-1}] \times [0.3 \text{ ppm C}_2\text{H}_6] / [3 \text{ ppm CH}_4] = +3.5\%$ .
- *Carbon monoxide*: the effect of carbon monoxide was not measured (as was the case of the above gases), but estimated from the spectral database HITRAN (Rothman et al., 2013).

### 3 Experimental methods

#### 3.1 The mobile methane and ethane laboratory

For the experiments in the Uintah basin, a small consumer sport utility vehicle is used as the mobile platform. An instrument (G2132-i, SN FCDS2004) is placed in the rear compartment of the vehicle. Power is supplied directly from the vehicle's 12 V DC electrical system via heavy gauge cables attached directly to the terminals of the vehi-

## Local and regional scale measurements of CH<sub>4</sub>, δ<sup>13</sup>CH<sub>4</sub>, and C<sub>2</sub>H<sub>6</sub> in the Uintah Basin

C. W. Rella et al.

Title Page

Abstract

Introduction

Conclusions

References

Tables

Figures

◀

▶

◀

▶

Back

Close

Full Screen / Esc

Printer-friendly Version

Interactive Discussion



cle battery. A 1000 W capacity DC to AC modified sine-wave inverter (Power Inverter 1000 W, West Marine, Watsonville, CA, USA) is used to supply power to the instrument, pumps, and other equipment in the vehicle. For safety, 40 A DC fuses are placed in line at the battery under the hood of the vehicle, and at the inverter, and care is taken to ensure that all the equipment is properly grounded to the vehicle frame.

A high precision GPS (R100, Hemisphere GPS, Scottsdale, Arizona, USA) is used for geolocation. The receiver antenna is affixed to the vehicle roof, and the 1 Hz positional data is integrated into the CRDS instrument data stream. A 2-D sonic anemometer is mounted 1.0 m above the roof to be out of the slipstream of the vehicle. Measurements of the wind, transverse and longitudinal to the car's orientation, are also integrated into the instrument data stream. Positional information from the GPS is used to remove the vehicle motion from the measured wind to determine the ground wind velocity.

### 3.2 Individual source signatures

The mobile laboratory was used to measure the source signatures (i.e., of δ<sup>13</sup>CH<sub>4</sub> and C<sub>2</sub>H<sub>6</sub>/CH<sub>4</sub> ratio) of individual emissions sources by directly measuring the composition of the plumes carried downwind of the source location. At driving speeds, typical plumes are traversed in just a couple of seconds. The isotope and ethane measurements are not of sufficient precision to allow for direct analysis of these very fast transients; for this reason, a custom flow system has been designed to allow for fast acquisition and slower re-analysis of atmospheric plumes. This system is shown in Fig. 11. A ~ 4 m long tube is mounted at about 0.15 m above the vehicle roof as the gas inlet, with a flow of about 1900 sccm. The instrument draws about 400 sccm of this gas, and a separate pump (Model S2000, Picarro Inc., Santa Clara, CA, USA) is used to draw the remaining gas flow (about 1500 sccm) from this common inlet through a 75 cc mixing volume and then a 15 m long, 8.0 mm I.D. aluminum tube with a volume of 770 cc. The propagation delay in this tube is about 30 s. This long tube is used as a gas storage container that at any point in time contains a gas sample corresponding to the

## Local and regional scale measurements of CH<sub>4</sub>, δ<sup>13</sup>CH<sub>4</sub>, and C<sub>2</sub>H<sub>6</sub> in the Uintah Basin

C. W. Rella et al.

Title Page

Abstract

Introduction

Conclusions

References

Tables

Figures

◀

▶

◀

▶

Back

Close

Full Screen / Esc

Printer-friendly Version

Interactive Discussion



last 30 s of measurements. The software controlling the flow system has two modes of operation. In “survey” mode, the instrument records data directly from the inlet, and the gas flows through the long tube toward the pump at a high flow rate. The software uses an automatic algorithm to detect if the vehicle has just passed through a plume: it identifies whether the concentration has crossed a given peak threshold (typically 1 ppm above background) and returning to within range of the background level (e.g., less than 0.3 ppm above the background level) within 15 s. If these criteria are met, then the flow is automatically switched to “replay” mode. In this case, the flow path is redirected such that the instrument draws directly from the far end of the long tube. The instrument flow is also reduced to about 60 sccm, which is 25 times lower than the “survey” mode flow through the storage tube. The key aspect of the long tube is that the plume concentration profile is substantially preserved in the tube, because the gas does not diffuse far along the length of the tube during the time of the measurement. This technology, called AirCore, was first developed by NOAA as a simple and effective way to measure the vertical profile of trace gases in the atmosphere (Karion et al., 2010; Tans, 2009). Once the gas in the tube is consumed (about 10 min), the flow automatically returns to survey mode.

Over a period of five days, 56 separate plume analyses were made in the Uintah basin. To quantify the isotopic signature of the sources, we have followed the analysis described by Miller and Tans (2003). The data from each plume measurement are analyzed with the following expression:

$$\delta_{\text{obs}}c_{\text{obs}} = \delta_{\text{s}}c_{\text{obs}} - c_{\text{bg}}(\delta_{\text{bg}} - \delta_{\text{s}}) \quad (16)$$

Where  $\delta_{\text{obs}}$  is the observed  $\delta^{13}\text{CH}_4$  signal,  $\delta_{\text{s}}$  is the  $\delta^{13}\text{CH}_4$  value of the source,  $\delta_{\text{bg}}$  is the  $\delta^{13}\text{CH}_4$  of the background gas,  $c_{\text{obs}}$  is the observed methane concentration, and  $c_{\text{bg}}$  is the background methane concentration. Thus, the isotope signature of the source is obtained from a linear fit of the product  $\delta_{\text{obs}}c_{\text{obs}}$  vs.  $c_{\text{obs}}$ . The ethane signatures of the individual sources were derived from the data from linear regressions of C<sub>2</sub>H<sub>6</sub> vs. CH<sub>4</sub> for each plume.

## Local and regional scale measurements of CH<sub>4</sub>, δ<sup>13</sup>CH<sub>4</sub>, and C<sub>2</sub>H<sub>6</sub> in the Uintah Basin

C. W. Rella et al.

Title Page

Abstract

Introduction

Conclusions

References

Tables

Figures

◀

▶

◀

▶

Back

Close

Full Screen / Esc

Printer-friendly Version

Interactive Discussion



Of the 56 individual source measurements, we have discarded measurements for which the uncertainty of the measurement was greater than  $\pm 7\%$  (1 sigma), leaving a total of 28 measurements. For each measurement, we used data from the on-board vehicle anemometer (after subtraction of the motion of the vehicle) to determine the wind direction and identify the source of the plume; by comparing to known locations of gas and oil wells (Uintah Map, 2013) we can categorize the sources as oil wells ( $N = 7$ ) or gas wells ( $N = 21$ ). These results are summarized in Fig. 12. From this figure we make two clear observations. First, the observed isotope ratios in the airborne plumes are consistent with the composition of the associated and non-associated gases as described in previous studies in the Uintah Basin (Rice et al., 1992) and from the work of Schoell (1980) and others. This is an important conclusion, as it means that there is not a significant degree of fractionation, either in  $C_2/C_1$  ratio or in  $\delta^{13}CH_4$ , associated with the fugitive emission processes that lead to the airborne natural gas plumes. Second, we note that the signature in the vicinity of the gas wells is distinct from the oil well plume signatures. The two populations can be separated using  $\delta^{13}CH_4$  (with plumes of  $> -48\%$  associated with gas wells), with the difference between the mean of the populations of  $15\%$  equal to three times the quadrature sum of the individual SD. We will use the two source signatures in the analysis of the regional atmospheric signal; this analysis is discussed below.

### 3.3 Regional atmospheric signature

The emissions sources of methane and ethane in the Uintah Basin together with the background concentrations of these gases determine the observed atmospheric signals. We first derive expressions relating the observed atmospheric concentrations and ratios given the background signals and the emissions quantities.

Consider first the emission of methane into the atmosphere. The observed concentration of methane is given by the expression below:

$$c_{\text{obs}} = c_{\text{bg}} + DE_c \quad (17)$$



## Local and regional scale measurements of CH<sub>4</sub>, δ<sup>13</sup>CH<sub>4</sub>, and C<sub>2</sub>H<sub>6</sub> in the Uintah Basin

C. W. Rella et al.

Title Page

Abstract

Introduction

Conclusions

References

Tables

Figures

◀

▶

◀

▶

Back

Close

Full Screen / Esc

Printer-friendly Version

Interactive Discussion



where  $c_{\text{obs}}$  is the observed mole fraction of methane (in absolute units, where e.g.  $2 \text{ ppm} = 2 \times 10^{-6}$ ),  $c_{\text{bg}}$  is the background mole fraction (same units),  $E_c$  is the emission rate of methane into the atmosphere, and  $D$  is an effective dilution factor for the atmosphere (in units of mole fraction per emission rate). Note that this expression is not exact: the expression holds only when  $c_{\text{obs}}$ ,  $c_{\text{bg}}$ , and  $DE_c \ll 1$ . This condition is met under all conditions typically observed in the atmosphere ( $c_{\text{obs}} < 2 \times 10^{-5} = 20 \text{ ppm}$ ). It is important to note that the term  $D$  is not a constant, but can vary over position (due to different spatial distribution of sources upwind of the vehicle) and time (as the atmospheric conditions change).

At any given point in space and time, the term  $DE_c$  represents the contribution of all upwind sources to the concentration measured at the point of the observer. The background concentration can be defined in multiple ways, depending on desired observing area or footprint of the measurement. In this paper, we are looking for regional emissions, so we consider the background to be the air entering the basin from the upwind direction.

We can write a similar expression to Eq. (17) for the tracer gas (in this case, either ethane or  $^{13}\text{CH}_4$ ):

$$e_{\text{obs}} = e_{\text{bg}} + DE_e \quad (18)$$

where  $e_{\text{obs}}$  and  $e_{\text{bg}}$  are mole fractions of the tracer gas for the observations and for background measurements. Note that we have assumed for a given point in space and time that the atmospheric dilution effect and transport (contained in the term  $D$ ) is the same for the primary gas (methane) and the tracer (ethane or  $^{13}\text{CH}_4$ ).

Solving to remove atmospheric dilution from these expressions, we find

$$\frac{e_{\text{obs}} - e_{\text{bg}}}{c_{\text{obs}} - c_{\text{bg}}} = \frac{E_e}{E_c} \equiv r_s \quad (19)$$

In which  $r_s$  is the overall emission ratio of all sources within the footprint of the observation. In general, we may express this overall source ratio in terms of the emissions

of each type of source. In Karion et al. (2013), the contributions of cattle and natural seepage to the total methane emissions was estimated to be 2.5 % production. For the purposes of this analysis, we ignore the contributions of these two sources, leaving two source types: oil wells and gas wells. We decompose the middle term of Eq. (19) into the two source types:

$$\frac{E_e}{E_c} = \frac{E_{e-oil} + E_{e-gas}}{E_{oil} + E_{gas}} = \frac{\frac{E_{e-oil}}{E_{oil}}E_{oil} + \frac{E_{e-gas}}{E_{gas}}E_{gas}}{E_{oil} + E_{gas}} \quad (20)$$

In this expression,  $E_{oil}$  and  $E_{gas}$  are the emission rates of methane from each source type, oil wells and gas wells; similarly,  $E_{e-oil}$  and  $E_{e-gas}$  are the tracer emissions from each source type. Defining  $r_{oil} = \frac{E_{e-oil}}{E_{oil}}$  and  $r_{gas} = \frac{E_{e-gas}}{E_{gas}}$ , we find:

$$r_s = \frac{r_{oil}E_{oil} + r_{gas}E_{gas}}{E_{oil} + E_{gas}} \quad (21)$$

Using Eq. (21), if we can measure  $r_s$  (the overall ratio of the tracer to methane observed in the atmosphere), and given the source signatures of oil and gas sources  $r_{oil}$  and  $r_{gas}$  observed in Fig. 12, we can determine the relative fraction of the emissions of oil and gas, without measuring the emission rates directly.

How can we determine the overall emission ratio  $r_s$ ? By regrouping terms in Eq. (19), and by defining  $r_{obs} = e_{obs}/c_{obs}$  and  $r_{bg} = e_{bg}/c_{bg}$ , we arrive at the following expression:

$$e_{obs} = r_s c_{obs} + (r_{bg} - r_s) c_{bg} \quad (22)$$

Note that the source emission ratio  $r_s$  is obtained from the slope of a plot of  $e_{obs}$  vs.  $c_{obs}$ . The equation constructed similarly to the Miller–Tans method for isotope analysis (Miller and Tans, 2003). In fact, this equation reduces to the Miller–Tans equation via

Local and regional scale measurements of CH<sub>4</sub>, δ<sup>13</sup>CH<sub>4</sub>, and C<sub>2</sub>H<sub>6</sub> in the Uintah Basin

C. W. Rella et al.

Title Page

Abstract

Introduction

Conclusions

References

Tables

Figures

◀

▶

◀

▶

Back

Close

Full Screen / Esc

Printer-friendly Version

Interactive Discussion



algebraic manipulation to convert the ratios  $r_s$ ,  $r_{\text{obs}}$ , and  $r_{\text{bg}}$  to delta notation via  $\delta = 1000 \left( \frac{r}{r_{\text{VPDB}}} - 1 \right)$ .

$$\delta_{\text{obs}} c_{\text{obs}} = \delta_s c_{\text{obs}} + (\delta_{\text{bg}} - \delta_s) c_{\text{bg}} \quad (23)$$

These expressions can be used to quantify the source signatures ( $r_s$  for ethane and  $\{\delta^{13}\text{CH}_4\}_s$ ) given the observations and the background values.

Our goal is to measure a representative sample of the air in the Basin from the mobile laboratory. With this goal in mind, we have designed a system that samples gas over long periods of time from the mobile lab, and enabling reanalysis of the gas in the lab, where careful calibration and longer measurement times can be brought to bear to improve the precision and accuracy of the measurements of  $\delta^{13}\text{CH}_4$  and ethane.

The sampling system is based on the AirCore concept, but with a much larger volume. The system is shown in Fig. 13. The top schematic shows the sampling system and the vehicle. Real-time measurements of the  $\text{CH}_4$  concentration are made during the drive, along with GPS coordinates and local wind speed and direction.

To ensure that the gas sampled in the storage tube is representative of the regional air, it is important to have a good understanding of the inlet flow of the system. Under constant pressure conditions at the inlet of the system, the flow at the inlet  $f_{\text{in}}$  is equal to the flow at the exit of the long storage tube  $f_{\text{out}}$ . However, the inlet pressure is not constant while in motion, due to altitude changes and dynamic pressure changes due to the Bernoulli Effect. These pressure changes will lead to flow changes at the inlet of the system, leading to uneven sampling of the regional air. We have constructed a complete air flow model that we have demonstrated matches observations. This model and associated experimental validation is described in the Supplement.

The bottom panel of Fig. 13 shows the laboratory reanalysis system. The reanalysis can occur at a much slower flow rate (about 17 sccm for experiments described here), leading to improved precision on the isotope and ethane analysis, and the overall accuracy and drift of the system is improved by using one or more calibration standards. For the measurements described here, we used a single cylinder at 1.85 ppm  $\text{CH}_4$  and

## Local and regional scale measurements of $\text{CH}_4$ , $\delta^{13}\text{CH}_4$ , and $\text{C}_2\text{H}_6$ in the Uintah Basin

C. W. Rella et al.

Title Page

Abstract

Introduction

Conclusions

References

Tables

Figures

◀

▶

◀

▶

Back

Close

Full Screen / Esc

Printer-friendly Version

Interactive Discussion



–47.5 ± 0.5‰ (a bottle of whole air collected and compressed at Niwot Ridge, Colorado) as the single standard. During each reanalysis period, we assumed that the drift of the instrument is in the concentration dependent term  $c_0(t)$  (Eq. 12).

To associate a particular measurement made in the laboratory during reanalysis to a specific location on the drive, it is necessary to properly re-synchronize the time axes, and to account for gas diffusion in the tube. This is accomplished using the following procedure:

1. The time axis during the “recording” phase is never adjusted.
2. The re-analysis time axis (called “replay” time) is first shifted by the time delay between the end of the recording and the beginning of the reanalysis.
3. The flow in the storage tube is reversed during reanalysis; for this reason, the replay time axis is reversed.
4. The time axis is compressed by the ratio of re-analysis flow to recording flow (or 17 sccm/88 sccm = 0.19).
5. To compare the methane signal measured during reanalysis to the recorded methane signal, a smoothing function is convolved with the recorded methane time series. This smoothing function is simply the Green’s function for one dimensional diffusion:

$$f(x) = \exp\left(-\frac{x^2}{4Dt_s}\right) \quad (24)$$

In this expression,  $x$  is distance along the length of the tube and  $t_s$  is the residence time of the gas at the location  $x$ , and we have used a diffusion constant  $D = 0.2 \text{ cm}^2 \text{ s}^{-1}$ . There are no free parameters in this smoothing function. It is important to note that other than gas diffusion (which conserves total methane), there are no adjustments made to the methane measurements during the recording phase or reanalysis phase.

Local and regional scale measurements of CH<sub>4</sub>, δ<sup>13</sup>CH<sub>4</sub>, and C<sub>2</sub>H<sub>6</sub> in the Uintah Basin

C. W. Rella et al.

Title Page

Abstract

Introduction

Conclusions

References

Tables

Figures

◀

▶

◀

▶

Back

Close

Full Screen / Esc

Printer-friendly Version

Interactive Discussion



## Local and regional scale measurements of CH<sub>4</sub>, δ<sup>13</sup>CH<sub>4</sub>, and C<sub>2</sub>H<sub>6</sub> in the Uintah Basin

C. W. Rella et al.

Title Page

Abstract

Introduction

Conclusions

References

Tables

Figures

◀

▶

◀

▶

Back

Close

Full Screen / Esc

Printer-friendly Version

Interactive Discussion



6. Finally, to account for flow differences in different parts of the drive, the replay time axis is compressed or expanded using a cubic spline function with 15 knots across the time axis (every 300 s), optimizing the time mismatch between the smoothed recorded methane signal and the reanalyzed signal.

5 The result of this procedure is shown in Fig. 14. The reanalyzed data reproduces the smoothed in-vehicle measurements well, except for the most narrow methane plumes observed during the drive (e.g., at  $t = 4800$  s). The mismatch in the vertical axis on these narrow plumes is due to (a) the fact that the instantaneous flow into the sampling tube is highly variable, leading to an under or over representation of that plume  
10 in the sampling tube, and (b) the two inlets are near to each other on the vehicle (within 0.5 m), but do not sample exactly the same location. The agreement between the time shift derived from the methane observations and the time shift predicted from the pressure/flow model (Supplement, Sect. B) indicates that the flow model is a good representation of the flow into the system.

15 Dozens of individual narrow plumes ( $< 10$  s in duration) are visible in Fig. 14. These plumes are due to sources that are relatively close to the vehicle ( $\lesssim 150$  m) during the drive. To the extent that these sources are representative of the overall distribution of sources in the region, these individual plumes do not present a problem, but if the sources are atypical, the regional emissions result derived from this analysis could  
20 have an error. We estimate the contribution of these individual sources in the regional signal using the following expression:

$$f_{\text{local}} = \frac{\int [c(t) - c_{15}(t)]}{\int [c(t) - c_0]} \quad (25)$$

25 where  $c(t)$  is the concentration observed during the drive,  $c_0$  is the minimum concentration observed on the drive (2.1 ppm in this case), and  $c_{15}(t)$  is the minimum concentration within  $\pm 15$  s of time  $t$ . Both integrals are performed over the entire drive. The integral in the numerator is near zero unless the vehicle encounters methane plumes that

## Local and regional scale measurements of CH<sub>4</sub>, δ<sup>13</sup>CH<sub>4</sub>, and C<sub>2</sub>H<sub>6</sub> in the Uintah Basin

C. W. Rella et al.

Title Page

Abstract

Introduction

Conclusions

References

Tables

Figures

◀

▶

◀

▶

Back

Close

Full Screen / Esc

Printer-friendly Version

Interactive Discussion



are narrower than about a minute of drive time. For slowly-varying signals, the moving baseline  $c_{15}(t)$  reduces the contribution to the integral. The integral in the denominator is used to normalize the signal. If we consider the example of a fairly constant baseline with narrow plumes (e.g., less than 15 s wide),  $f_{\text{local}}$  will be very close to 100 %. In contrast, a slowly varying methane signal with no narrow plumes will lead to  $f_{\text{local}}$  near 0 %. Using this expression, we calculate  $f_{\text{local}} = 10\%$ , indicating that 10 % of the observed signal in Fig. 14 is due to local influence, and thus that 90 % of the observed signal is a regional signal. Twenty-one plumes with a peak height greater than 0.5 ppm were identified, with an average amplitude = 5.6 ppm.

A total of three regional drives were performed in the winter of 2013, with a total distance travelled of 314 km. The regional fractions for these drives were 90, 92, and 91 %, for an average of 91 %. For each drive, data from the reanalysis is averaged in 5 min blocks, corresponding to a time resolution of about 1 min, or 1 km along the path of the vehicle. From this analysis, values for CH<sub>4</sub>, δ<sup>13</sup>CH<sub>4</sub>, and ethane are obtained.

Using the functional correspondence of the time axes of the recorded data and reanalyzed data, the isotope and ethane signatures are associated with specific geographic locations in the basin. A map of the Uintah basin, showing the locations of gas and oil wells is shown in Fig. 15, along with the recorded isotope signatures for the three drives. A clear geographic dependence of the isotope ratio can be seen, with the heaviest values observed in the primary gas production area in southeast of the basin, and the lightest values observed in the oil producing region in the west. The concentration signatures were also highest in the gas producing area, although, because the data were collected on different days with different atmospheric conditions, direct comparison is difficult.

Figure 16 shows a Keeling plot of the observed isotope ratios (left panel) and the ethane-to-methane ratio (right panel) from these drives.

We can make three clear observations from these data:

1. The regional isotope signatures are consistent with the gas wells as the predominant emissions source.

## Local and regional scale measurements of CH<sub>4</sub>, δ<sup>13</sup>CH<sub>4</sub>, and C<sub>2</sub>H<sub>6</sub> in the Uintah Basin

C. W. Rella et al.

2. The regional ethane-to-methane ratio is about 9.6%, which is close to the gas source average ratio of 11.8% (the centroid of the gas well ethane-to-methane ratio from Fig. 12), and significantly different than the oil well signature of 22.3% (also from Fig. 12), although we note that the uncertainty in the ethane ratios is very high for both populations (7.5 and 13%, respectively).

3. Even in the predominantly oil-producing western region (1 February drive), the observed isotope ratio, which shows significant deviation to lighter isotope values, implies that the observed signal is a mixture of nearby oil sources and the more distant gas sources.

Taken together, these observations provide strong evidence that the gas wells are the predominant source of methane in the Uintah basin. We note that these measurements were purposely made during a period of time when an atmospheric inversion was present in the Uintah Basin. There is only one opportunity for air to flow out of the basin (the Green River valley to the south), and the methane accumulated in the basin atmosphere over several days. It is therefore not surprising that the dominant emissions source signature (in this instance, the gas wells) would be visible throughout the basin, even in the western region.

To quantify the emission ratio, we apply the following algorithm. First, we consider each point in the left panel of Fig. 16, which corresponds to the isotope ratio at a specific location on one of the drives. From this isotope ratio, we can calculate a “local” isotope ratio at any position  $x$  on the path of the vehicle from the following expression based on Eq. (21):

$$\delta_s(x) = \frac{\delta_{\text{oil}}E_{\text{oil}}(x) + \delta_{\text{gas}}E_{\text{gas}}(x)}{E_{\text{oil}}(x) + E_{\text{gas}}(x)} \quad (26)$$

Title Page

Abstract

Introduction

Conclusions

References

Tables

Figures

◀

▶

◀

▶

Back

Close

Full Screen / Esc

Printer-friendly Version

Interactive Discussion



## Local and regional scale measurements of CH<sub>4</sub>, δ<sup>13</sup>CH<sub>4</sub>, and C<sub>2</sub>H<sub>6</sub> in the Uintah Basin

C. W. Rella et al.

Title Page

Abstract

Introduction

Conclusions

References

Tables

Figures

◀

▶

◀

▶

Back

Close

Full Screen / Esc

Printer-friendly Version

Interactive Discussion



If we define the fraction of emissions from gas wells observed at location  $x$  as  $R_{\text{gas}}(x) = \frac{E_{\text{gas}}(x)}{E_{\text{oil}}(x) + E_{\text{gas}}(x)}$ , and using the fact  $\frac{E_{\text{oil}}(x)}{E_{\text{oil}}(x) + E_{\text{gas}}(x)} = 1 - \frac{E_{\text{gas}}(x)}{E_{\text{oil}}(x) + E_{\text{gas}}(x)} = 1 - R_{\text{gas}}(x)$ , we find that

$$R_{\text{gas}}(x) = \frac{\delta_s(x) - \delta_{\text{oil}}}{\delta_{\text{gas}} - \delta_{\text{oil}}}.$$

To derive the total regional ratio  $R_{\text{gas}}$ , we need to perform a weighted sum over all locations in the basin:

$$R_{\text{gas}} = \frac{\sum_{\text{all } x} R_{\text{gas}}(x) E_{\text{tot}}(x)}{\sum_{\text{all } x} E_{\text{tot}}(x)} \quad (27)$$

It is difficult to quantify the local emissions  $E_{\text{tot}}(x)$  that contribute to a given regional signature. We do however know the concentration  $c(x)$ , which is the measured concentration along the path of the vehicle. Can  $c(x)$  be used as a proxy for  $E_{\text{tot}}(x)$ ? To the extent that the atmospheric dilution term  $D$  in Eq. (17) is substantially constant throughout the drive, and that sources are randomly distributed upwind of the vehicle, then the measured concentration enhancement  $c(x) - c_{\text{bg}}$  is a good proxy for the emissions rate, or

$$R_{\text{gas}} = \frac{\sum_{\text{all } x} R_{\text{gas}}(x) (c(x) - c_{\text{bg}})}{\sum_{\text{all } x} (c(x) - c_{\text{bg}})} \quad (28)$$

In which  $c_{\text{bg}}$  is the background value from which the concentration enhancement occurs. During the atmospheric inversion event, it is difficult to define a specific background value. For the purposes of this analysis, we assign the concentration measured at Niwot Ridge in February 2012 (Dlugokencky et al., 2014). The 2013 numbers were not yet available at the time this manuscript was prepared, but the effect of the new values on the result will be insignificant, given the very high enhancements observed during this study. The small fraction of the concentration enhancement that is due to sources outside the Uintah Basin will then contribute to the overall uncertainty of the emissions attribution; this contribution is difficult to quantify, but again, given the large



enhancements observed in this study. These sources of uncertainty in the background concentration and isotope ratio are captured in the Monte Carlo simulation, discussed below.

If we continue to use the assumption that the emission-weighted end members of gas and oil sources are  $-37.2$  and  $-57.3\%$ , respectively, we find that the overall emission ratio derived from each of the drives using Eq. (28) is 75, 95, and 93 % for each of the three drives (1, 3, and 9 February 2013). If each of the drives is weighted equally, we find that  $R_{\text{gas}} = 0.89$ . Alternatively, we take advantage of the fact that we drove certain segments of the drive on multiple days by adjusting the concentrations such that the observed concentration on all the drives are the same in these common segments of the paths. In that situation,  $R_{\text{gas}} = 0.86$  where the weighting factors for the three drives are 2.2, 1.0, and 3.6, respectively. Although the difference between the two results is small, we will use adopt this weighting in the uncertainty discussion below.

It is not a surprising result that the majority of methane emissions in the Uintah Basin are from natural gas wells. The 2012 emission study performed in the Uintah (Karion et al., 2013) focused on the gas producing eastern portion of the basin, but about 1000 of the 3000 oil wells in the basin. The western portion of the flight path used in that study traverses the western oil-producing region. This segment of the flight path does not show a significant methane enhancement, in support of the conclusion that the gas field is the dominant source of methane in the region.

To quantify the uncertainty in the fractional emissions estimate, we perform a Monte Carlo uncertainty analysis, by varying the following parameters (normally distributed) around their nominal values:  $\delta_{\text{gas}}$ ,  $\delta_{\text{oil}}$ ,  $\delta_{\text{bkgnd}}$ , and  $c_{\text{bkgnd}}$ . In Karion et al. (2013), no dominant single source of methane was found, in support of the idea that the emissions are due to an ensemble of many sources. We have thus assumed that the individual sources sampled directly are representative of the distribution of sources that comprise the total emissions. The variability in the gas and oil end members is given by the uncertainty in the means of each individual source distributions shown in Fig. 12, or  $\frac{\sigma_{\text{std}}}{\sqrt{N}}$  (Bevington and Robinson, 1969), assuming that the population of wells sampled

## Local and regional scale measurements of $\text{CH}_4$ , $\delta^{13}\text{CH}_4$ , and $\text{C}_2\text{H}_6$ in the Uintah Basin

C. W. Rella et al.

Title Page

Abstract

Introduction

Conclusions

References

Tables

Figures

◀

▶

◀

▶

Back

Close

Full Screen / Esc

Printer-friendly Version

Interactive Discussion



## Local and regional scale measurements of CH<sub>4</sub>, δ<sup>13</sup>CH<sub>4</sub>, and C<sub>2</sub>H<sub>6</sub> in the Uintah Basin

C. W. Rella et al.

Title Page

Abstract

Introduction

Conclusions

References

Tables

Figures

◀

▶

◀

▶

Back

Close

Full Screen / Esc

Printer-friendly Version

Interactive Discussion



is representative of all the wells contributing to the emissions. In addition, we have assumed an uncertainty in  $\delta_{\text{bkgnd}}$  and  $C_{\text{bkgnd}}$  of 1 ‰ and 0.1 ppm, respectively; the primary source of the uncertainty in the background parameter is due to the fact, because of the atmospheric inversion, it is not possible to define a clear background for the regional enhancements. For this set of parameters, we find that  $R_{\text{gas}} = 0.86 \pm 0.07$  ( $1\sigma$ ), where 95 % of the Monte Carlo realizations have  $R_{\text{gas}} > 0.75$ . The contributions of  $\delta_{\text{gas}}$  and  $\delta_{\text{bkgnd}}$  to the total uncertainty are approximately equal, and together account for 90 % of the total uncertainty of 0.07.

If the isotope ratios of the sources sampled are not representative of the emissions-weighted distribution of well signatures, then uncertainty in the mean of the sampled distribution underestimates the uncertainty in the centroid of the full population. The uncertainty in the end members should be increased to encompass the populations that were not sampled. Assuming that the population is at least *somewhat* representative, and noting that the observed range in isotope values and ethane ratios is typical of oil and gas producing geological formations, then the SD of the sampled distribution should represent a reasonable upper limit for the uncertainty. In this situation, a substantial fraction of the Monte Carlo realizations are non-physical; i.e., the isotope ratios observed in the regional sampling can exceed the simulated gas well end member, leading to calculated emission ratios that exceed 1 at times. However, even with these highly uncertain end member populations, > 98 % of the realizations predict that  $R_{\text{gas}} > 0.5$ , and 80 % of the realizations indicate that  $R_{\text{gas}} > 0.7$ , providing a highly confident lower bound for the emission ratio  $R_{\text{gas}}$ .

Finally, we note that the three drives that contributed to this study are not necessarily representative of the total air mass in the basin. We can obtain one estimate of this sampling uncertainty by noting that the drive in the oil-producing region lead to an estimate of 75 % for the emission ratio, and drives in the gas-producing region lead to estimates of 93 and 95 %, for a total span of about  $\pm 10$  % at most.

## 4 Summary

In this paper, we present a comprehensive approach to emissions attribution, using an innovative CH<sub>4</sub>, δ<sup>13</sup>CH<sub>4</sub>, and C<sub>2</sub>H<sub>6</sub> instrument based on cavity ring down spectroscopy (CRDS). The design and performance of the analyzer is presented in detail.

We have demonstrated that with proper calibration, the instrument can deliver high quality δ<sup>13</sup>CH<sub>4</sub> measurements with a precision that is comparable to isotope ratio mass spectrometry. The instrument is compact and rugged, and can be deployed in remote field stations or mobile platforms with a minimal amount of user attention.

As an example of the type of research that can be performed with this instrument, field measurements were performed in the Uintah Basin (Utah, USA) in the winter of 2013, using a mobile lab equipped with the CRDS analyzer, a high-accuracy GPS, a sonic anemometer, and a novel onboard gas storage and playback system. With an extremely small population and almost no other sources of methane and ethane other than oil and gas extraction activities, the Uintah Basin represents an ideal location to investigate and validate new measurement methods of atmospheric methane and ethane. We present the results of measurements of the fugitive emissions from 23 natural gas wells and 6 oil wells in the region. The δ<sup>13</sup>CH<sub>4</sub> and C<sub>2</sub>H<sub>6</sub> signatures that we observe are consistent with the signatures present in the ground. Furthermore, regional measurements of the atmospheric CH<sub>4</sub>, δ<sup>13</sup>CH<sub>4</sub>, and C<sub>2</sub>H<sub>6</sub> signatures throughout the basin have been made, using continuous atmospheric sampling into a 450 m long tube. These measurements suggest that 86 ± 7 % of the total emissions in the basin are from natural gas production.

**The Supplement related to this article is available online at doi:10.5194/amtd-8-4859-2015-supplement.**

### Local and regional scale measurements of CH<sub>4</sub>, δ<sup>13</sup>CH<sub>4</sub>, and C<sub>2</sub>H<sub>6</sub> in the Uintah Basin

C. W. Rella et al.

Title Page

Abstract

Introduction

Conclusions

References

Tables

Figures

◀

▶

◀

▶

Back

Close

Full Screen / Esc

Printer-friendly Version

Interactive Discussion



*Acknowledgements.* The authors would like to thank Colm Sweeney, Gaby Petron, Anna Karion, Sonja Wolter, Tim Newberger, and Bruce Vaughn for experimental support and helpful scientific discussions during this project.

## References

- 5 Allan, D. W.: Statistics of atomic frequency standards, P. IEEE, 54, 221–230, 1966.
- Alvarez, R. A., Pacalab, S. W., Winebrake, J. J., Chameides, W. L., and Hamburg, S. P.: Greater focus needed on methane leakage from natural gas infrastructure, P. Natl. Acad. Sci. USA, 109, 6435–6440, doi:10.1073/pnas.1202407109, 2012.
- 10 Bevington, P. R. and Robinson, D. K.: Data Reduction and Error Analysis for the Physical Sciences, vol. 336, McGraw-Hill, New York, 1969.
- Bräunlich, M., Aballain, O., Marik, T., Jöckel, P., Brenninkmeijer, C. A., Chappellaz, J., and Sturges, W. T.: Changes in the global atmospheric methane budget over the last decades inferred from  $^{13}\text{C}$  and D isotopic analysis of Antarctic firn air, J. Geophys. Res.-Atmos., 106, 20465–20481, 2001.
- 15 Chen, H., Winderlich, J., Gerbig, C., Hofer, A., Rella, C. W., Crosson, E. R., Van Pelt, A. D., Steinbach, J., Kolle, O., Beck, V., Daube, B. C., Gottlieb, E. W., Chow, V. Y., Santoni, G. W., and Wofsy, S. C.: High-accuracy continuous airborne measurements of greenhouse gases ( $\text{CO}_2$  and  $\text{CH}_4$ ) using the cavity ring-down spectroscopy (CRDS) technique, Atmos. Meas. Tech., 3, 375–386, doi:10.5194/amt-3-375-2010, 2010.
- 20 Coplen, T. B., Brand, W. A., Gehre, M., Gröning, M., Meijer, H. A., Toman, B., and Verkoouteren, R. M.: After two decades a second anchor for the VPDB  $\delta^{13}\text{C}$  scale, Rapid Commun. Mass Sp., 20, 3165–3166, 2005.
- Crosson, E. R.: A cavity ring-down analyzer for measuring atmospheric levels of methane, carbon dioxide, and water vapor, Appl. Phys. B-Lasers O., 92, 403–408, doi:10.1007/s00340-008-3135-y, 2008.
- 25 Dlugokencky, E. J., Lang, P. M., Crotwell, A. M., Masarie, K. A., and Crotwell, M. J.: Atmospheric Methane Dry Air Mole Fractions from the NOAA ESRL Carbon Cycle Cooperative Global Air Sampling Network, 1983–2013, Version: 2014-06-24, available at: ftp://aftp.cmdl.noaa.gov/data/trace\_gases/ch4/flask/surface/ch4\_nwr\_surface-flask\_1\_ccgg\_month.txt, last access: 29 July 2014.
- 30

## Local and regional scale measurements of $\text{CH}_4$ , $\delta^{13}\text{CH}_4$ , and $\text{C}_2\text{H}_6$ in the Uintah Basin

C. W. Rella et al.

Title Page

Abstract

Introduction

Conclusions

References

Tables

Figures

◀

▶

◀

▶

Back

Close

Full Screen / Esc

Printer-friendly Version

Interactive Discussion





## Local and regional scale measurements of CH<sub>4</sub>, δ<sup>13</sup>CH<sub>4</sub>, and C<sub>2</sub>H<sub>6</sub> in the Uintah Basin

C. W. Rella et al.

Title Page

Abstract

Introduction

Conclusions

References

Tables

Figures

◀

▶

◀

▶

Back

Close

Full Screen / Esc

Printer-friendly Version

Interactive Discussion

Weiss, R. F., Williams, J. E., and Zeng, G.: Three decades of global methane sources and sinks, *Nat. Geosci.*, 6, 813–823, 2013.

Levin, I., Glatzel-Mattheier, H., Marik, T., Cuntz, M., Schmidt, M., and Worthy, D. E.: Verification of German methane emission inventories and their recent changes based on atmospheric observations, *J. Geophys. Res.*, 104, 3447–3456, doi:10.1029/1998JD100064, 1999.

Lowe, D., White, J., Levin, I., Bergamaschi, P., Wahlen, M., and Miller, J.: Stable isotope measurement techniques for atmospheric greenhouse gases, International Atomic Energy Agency, available at: <http://www-naweb.iaea.org/napc/ih/documents/TECDOCS/TECDOC%201268%20Atmospheric%20greenhouse%20gases%202002.pdf>, 2002.

Marrero, T. R. and Mason, E. A.: Gaseous diffusion coefficients, *J. Phys. Chem. Ref. Data*, 1, 3–118, 1972.

Mikaloff Fletcher, S. E., Tans, P. P., Bruhwiler, L. M., Miller, J. B., and Heimann, M.: CH<sub>4</sub> sources estimated from atmospheric observations of CH<sub>4</sub> and its <sup>13</sup>C/<sup>12</sup>C isotopic ratios: 1. Inverse modeling of source processes, *Global Biogeochem. Cy.*, 18, GB4004, doi:10.1029/2004GB002223, 2004a.

Mikaloff Fletcher, S. E., Tans, P. P., Bruhwiler, L. M., Miller, J. B., and Heimann, M.: CH<sub>4</sub> sources estimated from atmospheric observations of CH<sub>4</sub> and its <sup>13</sup>C/<sup>12</sup>C isotopic ratios: 2. Inverse modeling of CH<sub>4</sub> fluxes from geographical regions, *Global Biogeochem. Cy.*, 18, GB4005, doi:10.1029/2004GB002224, 2004b.

Miller, J. B. and Tans, P. P.: Calculating isotopic fractionation from atmospheric measurements at various scales, *Tellus B*, 55, 207–214, 2003.

Mischler, J. A., Sowers, T. A., Alley, R. B., Battle, M., McConnell, J. R., Mitchell, L., Popp, T., Sofen, E., and Spencer, M. K.: Carbon and hydrogen isotopic composition of methane over the last 1000 years, *Global Biogeochem. Cy.*, 23, GB4024, doi:10.1029/2009GB003460, 2009.

Myhre, G., Shindell, D., Bréon, F.-M., Collins, W., Fuglestedt, J., Huang, J., Koch, D., Lamarque, J.-F., Lee, D., Mendoza, B., Nakajima, T., Robock, A., Stephens, G., Takemura, T., and Zhang, H.: Anthropogenic and natural radiative forcing, in: *Climate Change 2013: the Physical Science Basis. Contribution of Working Group I to the Fifth Assessment Report of the Intergovernmental Panel on Climate Change*, edited by: Stocker, T. F., Qin, D., Plattner, G.-K., Tignor, M., Allen, S. K., Boschung, J., Nauels, A., Xia, Y., Bex, V., and Midgley, P. M., Cambridge University Press, Cambridge, UK, New York, NY, USA, 659–740, 2013.



## Local and regional scale measurements of CH<sub>4</sub>, δ<sup>13</sup>CH<sub>4</sub>, and C<sub>2</sub>H<sub>6</sub> in the Uintah Basin

C. W. Rella et al.

Title Page

Abstract

Introduction

Conclusions

References

Tables

Figures

◀

▶

◀

▶

Back

Close

Full Screen / Esc

Printer-friendly Version

Interactive Discussion



resources of the Uinta Basin, Utah and Colorado, edited by: Fouch, T. D., Vito F. N., and Chidsey Jr., T. C., Utah Geological Association Guidebook, 20, 95–110, 1992.

Richardson, S. J., Miles, N. L., Davis, K. J., Crosson, E. R., Rella, C. W., and Andrews, A. E.: Field testing of cavity ring-down spectroscopy analyzers measuring carbon dioxide and water vapor, *J. Atmos. Ocean. Tech.*, 29, 397–406, 2012.

Rothman, L. S., Gordon, I. E., Babikov, Y., Barbe, A., Chris Benner, D., Bernath, P. F., Birk, M., Bizzocchi, L., Boudon, V., Brown, L. R., Campargue, A., Chance, K., Cohen, E. A., Coudert, L. H., Devi, V. M., Drouin, B. J., Fayt, A., Flaud, J.-M., Gamache, R. R., Harrison, J. J., Hartmann, J.-M., Hill, C., Hodges, J. T., Jacquemart, D., Jolly, A., Lamouroux, J., Le Roy, R. J., Li, G., Long, D. A., Lyulin, O. M., Mackie, C. J., Massie, S. T., Mikhailenko, S., Müller, H. S. P., Naumenko, O. V., Nikitin, A. V., Orphal, J., Perevalov, V., Perrin, A., Polovtseva, E. R., Richard, C., Smith, M. A. H., Starikova, E., Sung, K., Tashkun, S., Tennyson, J., Toon, G. C., Tyuterev, V. G., and Wagner, G.: The HITRAN2012 molecular spectroscopic database, *J. Quant. Spectrosc. Ra.*, 130, 4–50, 2013.

Schnell, R. C., Oltmans, S. J., Johnson, B. J., and Neely III, R. R.: The Anatomy of Wintertime Photochemical Ozone Production Events in the Upper Green River, WY and Uintah, UT Natural Gas Fields, in: AGU Fall Meeting Abstracts, San Francisco, USA, 3–7 December 2012, Vol. 1, p. 5, 2012.

Schoell, M.: The hydrogen and carbon isotopic composition of methane from natural gases of various origins, *Geochim. Cosmochim. Ac.*, 44, 649–661, doi:10.1016/0016-7037(80)90155-6, 1980.

Simpson, I. J., Andersen, M. P. S., Meinardi, S., Bruhwiler, L., Blake, N. J., Helmig, D., Sherwood Rowland, F., and Blake, D. R.: Long-term decline of global atmospheric ethane concentrations and implications for methane, *Nature*, 488, 490–494, 2012.

Smith, L. K., Lewis Jr., W. M., Chanton, J. P., Cronin, G., and Hamilton, S. K.: Methane emissions from the Orinoco River floodplain, Venezuela, *Biogeochemistry*, 51, 113–140, 2000.

Tans, P. P.: US Patent No. 7,597,014, US Patent and Trademark Office, Washington, DC, 2009. UBETS Report: Final Report: Uintah Basin Energy and Transportation Study, available at: [www.utssd.utah.gov/documents/ubetsreport.pdf](http://www.utssd.utah.gov/documents/ubetsreport.pdf) (last access: 18 June 2014), 2013.

Uintah Map: Uintah County Oil and Gas Wells, created 4/16/2013, available at: <http://www.co.uintah.ut.us/gis/Oil%20and%20Gas%20Wells.pdf> (last access: 4 July 2014), 2013.



## Local and regional scale measurements of CH<sub>4</sub>, δ<sup>13</sup>CH<sub>4</sub>, and C<sub>2</sub>H<sub>6</sub> in the Uintah Basin

C. W. Rella et al.

Title Page

Abstract

Introduction

Conclusions

References

Tables

Figures

◀

▶

◀

▶

Back

Close

Full Screen / Esc

Printer-friendly Version

Interactive Discussion



Utah Well Information Query: State of Utah Department of Natural Resources Division of Oil Gas and Mining, Well Information Query, available at: [http://oilgas.ogm.utah.gov/Data\\_Center/LiveData\\_Search/well\\_information.htm](http://oilgas.ogm.utah.gov/Data_Center/LiveData_Search/well_information.htm) (last access: February 2013), 2012.

Varghese, P. L. and Hanson, R. K.: Collisional narrowing effects on spectral line shapes measured at high resolution, *Appl. Optics*, 23, 2376–2385, doi:10.1364/AO.23.002376, 1984.

Werner, R. A. and Brand, W. A.: Referencing strategies and techniques in stable isotope ratio analysis, *Rapid Commun. Mass Sp.*, 15, 501–519, 2001.

Winderlich, J., Chen, H., Gerbig, C., Seifert, T., Kolle, O., Lavrič, J. V., Kaiser, C., Höfer, A., and Heimann, M.: Continuous low-maintenance CO<sub>2</sub>/CH<sub>4</sub>/H<sub>2</sub>O measurements at the Zotino Tall Tower Observatory (ZOTTO) in Central Siberia, *Atmos. Meas. Tech.*, 3, 1113–1128, doi:10.5194/amt-3-1113-2010, 2010.

Xiao, Y., Logan, J. A., Jacob, D. J., Hudman, R. C., Yantosca, R., and Blake, D. R.: Global budget of ethane and regional constraints on US sources, *J. Geophys. Res.-Atmos.*, 113, D21306, doi:10.1029/2007JD009415, 2008.

Zazzeri, G., Lowry, D., Fisher, R. E., France, J. L., Lanoisellé, M., Nisbet, E. G.: Plume mapping and isotopic characterisation of anthropogenic methane sources, *Atmos. Environ.*, 110, 151–162, doi:10.1016/j.atmosenv.2015.03.029, 2015.

## Local and regional scale measurements of CH<sub>4</sub>, δ<sup>13</sup>CH<sub>4</sub>, and C<sub>2</sub>H<sub>6</sub> in the Uintah Basin

C. W. Rella et al.

**Table 1.** Summary of cross-interference due to direct absorption on δ<sup>13</sup>CH<sub>4</sub> from a variety of species. Reported as a slope for linear cross-interference, and as a range (95 % coverage factor) for non-linear cross-interference over a specified range of concentration of the interfering species. A positive sign indicates that the value of δ<sup>13</sup>CH<sub>4</sub> reported by the instrument is more positive than the actual value. See the text for more information.

Gas species	Chemical formula	Estimated effect on δ <sup>13</sup> CH <sub>4</sub>	notes
Oxygen	O <sub>2</sub>	+0.173 ± 0.023 ‰‰ <sup>-1</sup> O <sub>2</sub>	Indep. of CH <sub>4</sub> conc.
Argon	Ar	≈ +0.4 ‰‰ <sup>-1</sup> Ar	Indep. of CH <sub>4</sub> conc.; est. from O <sub>2</sub> dependence, using Nara et al. (2012)
Water vapor	H <sub>2</sub> O	< ± 1 ‰	0–2.5 % H <sub>2</sub> O and 1–15 ppm CH <sub>4</sub>
Carbon Dioxide	CO <sub>2</sub>	< ± 0.5 ‰	200–1800 ppm CO <sub>2</sub> and 1–15 ppm CH <sub>4</sub>
Ethane	C <sub>2</sub> H <sub>6</sub>	+35 ‰‰ ppm CH <sub>4</sub> (ppm C <sub>2</sub> H <sub>6</sub> ) <sup>-1</sup>	Inversely prop. to CH <sub>4</sub> conc.
Ammonia*	NH <sub>3</sub>	-7.0 ‰‰ ppm CH <sub>4</sub> (ppm NH <sub>3</sub> ) <sup>-1</sup>	Inversely prop. to CH <sub>4</sub> conc.
Hydrogen Sulfide	H <sub>2</sub> S	< 0.2 ‰‰ ppm CH <sub>4</sub> (ppm H <sub>2</sub> S) <sup>-1</sup>	Inversely prop. to CH <sub>4</sub> conc.
Methyl Mercaptan	CH <sub>3</sub> SH	< 6 ‰‰ ppm CH <sub>4</sub> (ppm CH <sub>3</sub> ) <sup>-1</sup> SH	Inversely prop. to CH <sub>4</sub> conc.
Propane	C <sub>3</sub> H <sub>8</sub>	< 0.1 ‰‰ ppm CH <sub>4</sub> (ppm C <sub>3</sub> H <sub>8</sub> ) <sup>-1</sup>	Inversely prop. to CH <sub>4</sub> conc.
Butane	C <sub>4</sub> H <sub>10</sub>	< 0.1 ‰‰ ppm CH <sub>4</sub> (ppm C <sub>4</sub> H <sub>10</sub> ) <sup>-1</sup>	Inversely prop. to CH <sub>4</sub> conc.
Ethylene	C <sub>2</sub> H <sub>4</sub>	+20 ‰‰ ppm CH <sub>4</sub> (ppm C <sub>2</sub> H <sub>4</sub> ) <sup>-1</sup>	Inversely prop. to CH <sub>4</sub> conc.
Carbon Monoxide	CO	< 0.02 ‰‰ ppm CH <sub>4</sub> (ppm CO) <sup>-1</sup>	Est. from HITRAN database (Rothman et al., 2013)

\* Ammonia also has a known strong cross interference on the ethane measurement.

Title Page

Abstract

Introduction

Conclusions

References

Tables

Figures

◀

▶

◀

▶

Back

Close

Full Screen / Esc

Printer-friendly Version

Interactive Discussion



## Local and regional scale measurements of CH<sub>4</sub>, δ<sup>13</sup>CH<sub>4</sub>, and C<sub>2</sub>H<sub>6</sub> in the Uintah Basin

C. W. Rella et al.

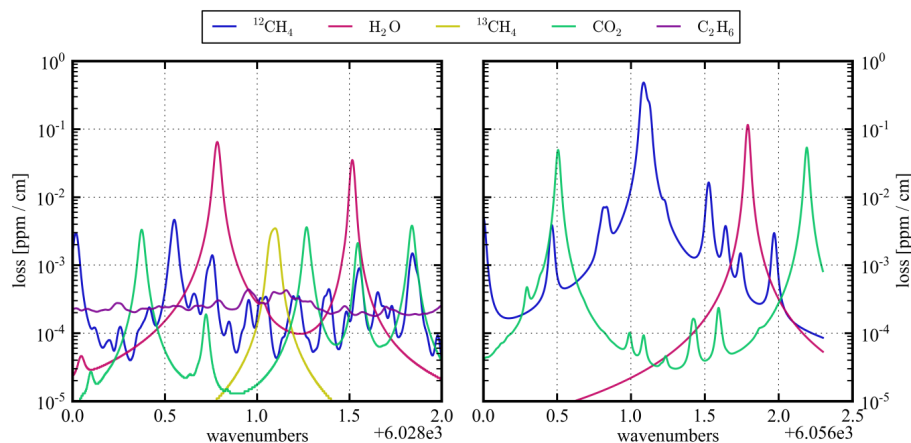


**Figure 1.** Spectra of key species in the frequency ranges employed in the spectrometer, displaying loss on a log scale vs. optical frequency in wavenumbers for the low frequency region (left panel) and high frequency region (right panel). The spectra for methane (both isotopologues, concentration of 2 ppm), water vapor (1 %), and carbon dioxide (400 ppm) are obtained from the HITRAN spectral database (Rothman et al., 2013), for a pressure of 148 Torr and  $T = 45^\circ\text{C}$ . The ethane spectrum (for a concentration of 1 ppm) was obtained experimentally using the CRDS spectrometer from a 400 ppm bottle.

Title Page

Abstract

Introduction

Conclusions

References

Tables

Figures

◀

▶

◀

▶

Back

Close

Full Screen / Esc

Printer-friendly Version

Interactive Discussion

## Local and regional scale measurements of CH<sub>4</sub>, δ<sup>13</sup>CH<sub>4</sub>, and C<sub>2</sub>H<sub>6</sub> in the Uintah Basin

C. W. Rella et al.

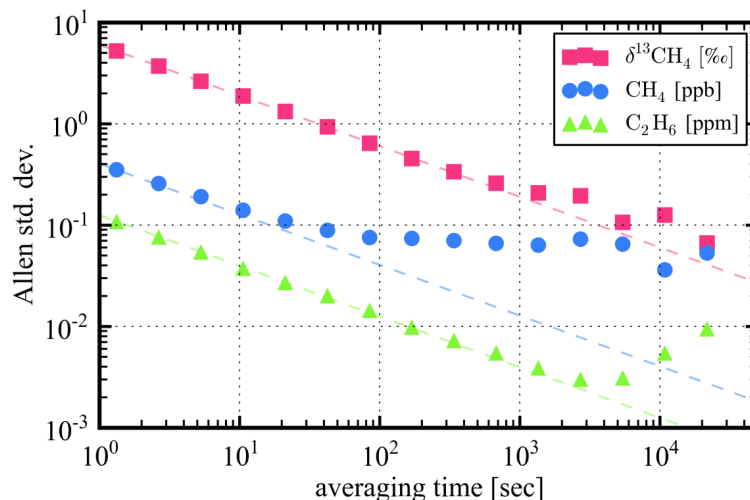


**Figure 2.** Allan standard deviation for δ<sup>13</sup>CH<sub>4</sub>, CH<sub>4</sub>, and C<sub>2</sub>H<sub>6</sub> collected over 18 h, in units of ‰, ppb, and ppm, as noted in the legend. The precision of the instrument is about 0.4 ppb for CH<sub>4</sub> in a 1.2 s measurement, and below 1.0 ‰ for δ<sup>13</sup>CH<sub>4</sub> in a minute of averaging. The ethane measurement precision is about 20 ppb in 1 min. The latter two quantities follow a square root averaging law for 1 h or more of averaging.

Title Page

Abstract

Introduction

Conclusions

References

Tables

Figures

◀

▶

◀

▶

Back

Close

Full Screen / Esc

Printer-friendly Version

Interactive Discussion



## Local and regional scale measurements of CH<sub>4</sub>, δ<sup>13</sup>CH<sub>4</sub>, and C<sub>2</sub>H<sub>6</sub> in the Uintah Basin

C. W. Rella et al.

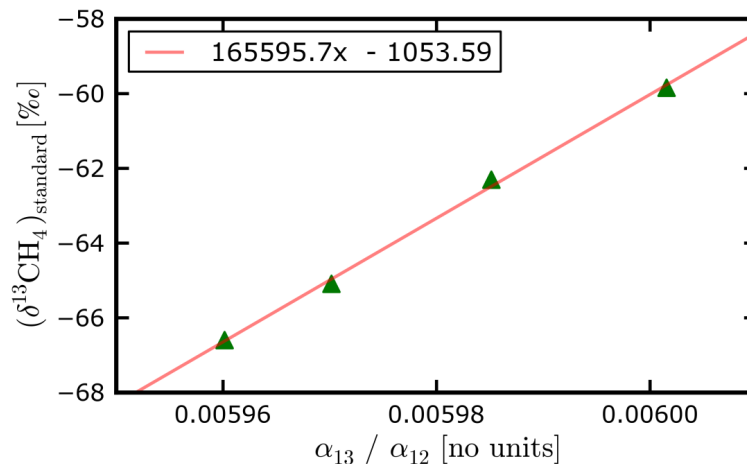


**Figure 3.** Isotope calibration experiment, using samples prepared for this work and then analyzed at a commercial isotope laboratory. The  $x$  axis shows the raw loss ratio provided by the instrument, and the  $y$  axis are the results of the external analysis. The linear fit coefficients have been applied to all CRDS instruments that use these spectroscopic lines for  $\delta^{13}\text{CH}_4$  quantification.

[Title Page](#)[Abstract](#)[Introduction](#)[Conclusions](#)[References](#)[Tables](#)[Figures](#)[◀](#)[▶](#)[◀](#)[▶](#)[Back](#)[Close](#)[Full Screen / Esc](#)[Printer-friendly Version](#)[Interactive Discussion](#)

**Local and regional scale measurements of CH<sub>4</sub>, δ<sup>13</sup>CH<sub>4</sub>, and C<sub>2</sub>H<sub>6</sub> in the Uintah Basin**

C. W. Rella et al.

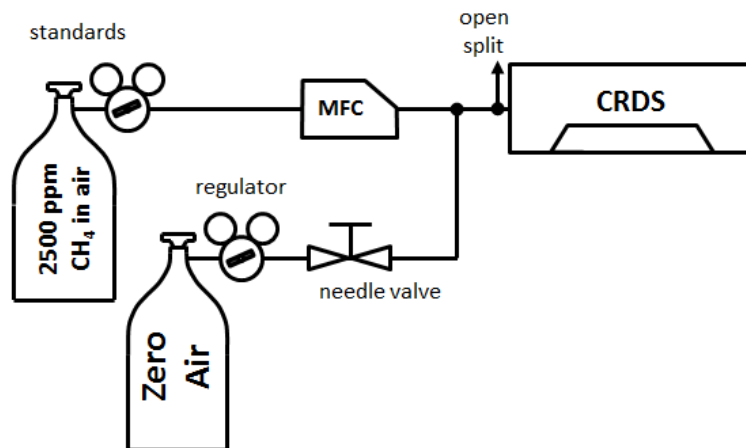


**Figure 4.** Setup for measuring dilute mixtures of 2500 ppm standards. The MFC was set to flows ranging from 2 to 20 sccm. The needle valve was set to  $\sim 1000$  sccm dilution, for a concentration range of 2–20 ppm delivered to the instrument.

Title Page

Abstract

Introduction

Conclusions

References

Tables

Figures

◀

▶

◀

▶

Back

Close

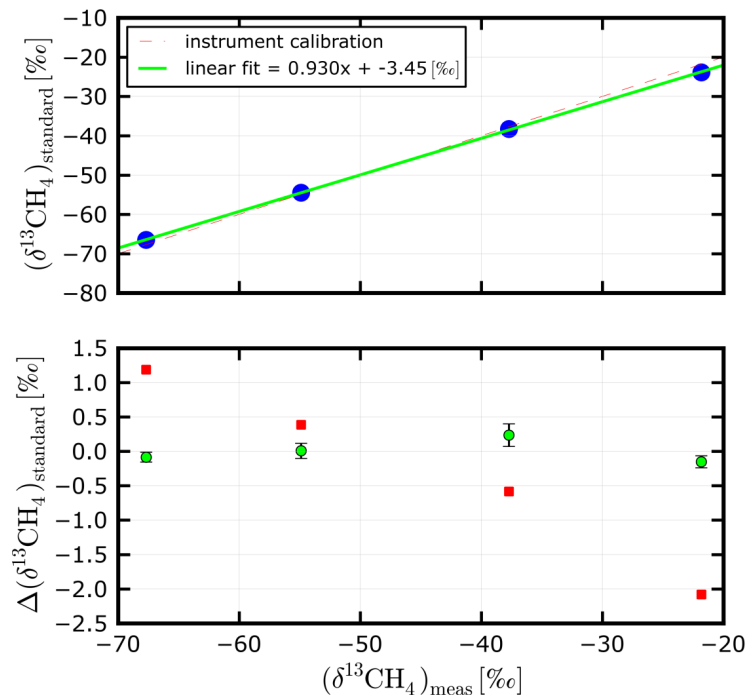
Full Screen / Esc

Printer-friendly Version

Interactive Discussion

## Local and regional scale measurements of CH<sub>4</sub>, δ<sup>13</sup>CH<sub>4</sub>, and C<sub>2</sub>H<sub>6</sub> in the Uintah Basin

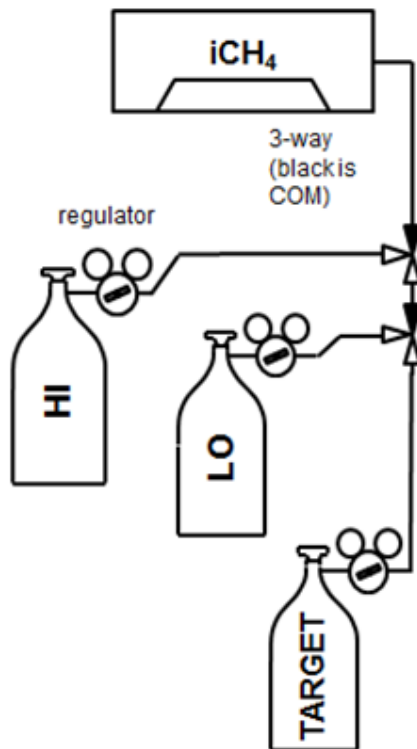
C. W. Rella et al.



**Figure 5.** Results of the validation calibration experiment. Top panel: blue circles: measured isotope ratio ( $x$  values) vs. standard values from the vendor. Green line: linear fit to these data. Red dashed line: standard instrument calibration ( $A = 165\,595.7$  and  $B = -1053.61$ ), and including the loss nonlinearity term  $\beta$  and an optimized overall loss offset  $\alpha_0$  of  $-0.0103$  ppb  $\text{cm}^{-1}$ . Bottom panel: green circles: residuals from the green line in the top panel. The error bars indicate the SD of the four concentration measurements between 1.9 and 15 ppm for each isotope standard, but do not include the uncertainty in the standard value of 0.2%. Red squares: difference between the measured value using the standard instrument calibration and the standard value.

**Local and regional scale measurements of CH<sub>4</sub>, δ<sup>13</sup>CH<sub>4</sub>, and C<sub>2</sub>H<sub>6</sub> in the Uintah Basin**

C. W. Rella et al.

**Figure 6.** Setup for drift correction testing.

Title Page

Abstract

Introduction

Conclusions

References

Tables

Figures

◀

▶

◀

▶

Back

Close

Full Screen / Esc

Printer-friendly Version

Interactive Discussion





## Local and regional scale measurements of CH<sub>4</sub>, δ<sup>13</sup>CH<sub>4</sub>, and C<sub>2</sub>H<sub>6</sub> in the Uintah Basin

C. W. Rella et al.

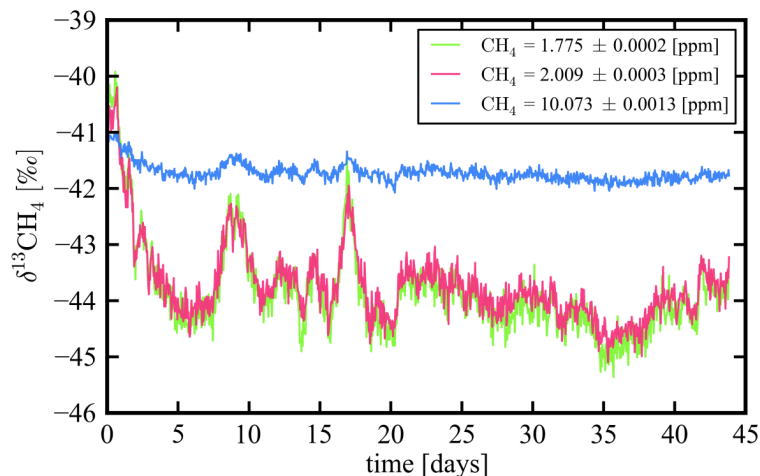


**Figure 7.** Measured isotope ratio on three bottles, HI (10.1 ppmCH<sub>4</sub> and δ<sup>13</sup>CH<sub>4</sub> = -41.7‰, blue line), LO (1.78 ppm and δ<sup>13</sup>CH<sub>4</sub> = -44.5‰, green line), and Target (2.01 ppm, unknown isotope ratio, red line).

[Title Page](#)[Abstract](#)[Introduction](#)[Conclusions](#)[References](#)[Tables](#)[Figures](#)[◀](#)[▶](#)[◀](#)[▶](#)[Back](#)[Close](#)[Full Screen / Esc](#)[Printer-friendly Version](#)[Interactive Discussion](#)

## Local and regional scale measurements of $\text{CH}_4$ , $\delta^{13}\text{CH}_4$ , and $\text{C}_2\text{H}_6$ in the Uintah Basin

C. W. Rella et al.

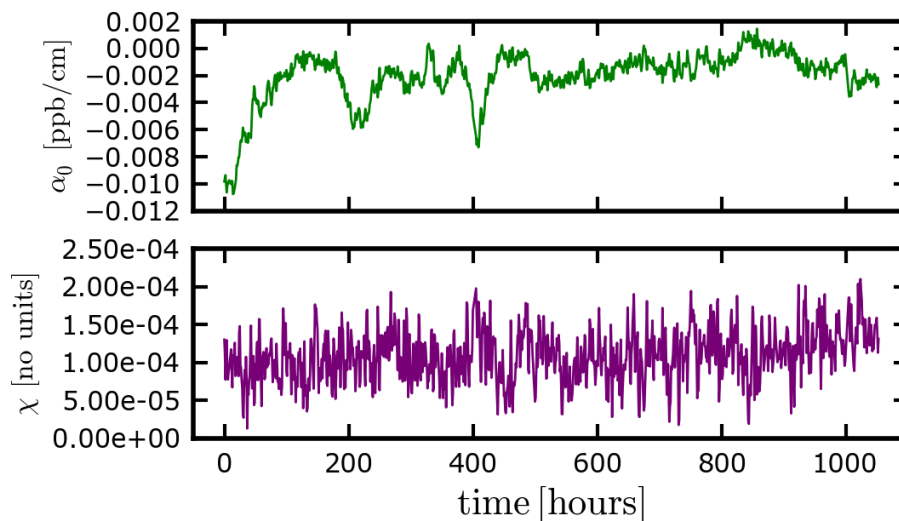


**Figure 8.** Measurements of the drift correction parameters  $\chi(t_i)$  (bottom panel) and  $\alpha_0(t_i)$  (top panel), measured from the HI and LO bottles as described in the text. At 2 ppm  $\text{CH}_4$ , the parameter  $\alpha_0(t_i)$  dominates the drift.

[Title Page](#)[Abstract](#)[Introduction](#)[Conclusions](#)[References](#)[Tables](#)[Figures](#)[◀](#)[▶](#)[◀](#)[▶](#)[Back](#)[Close](#)[Full Screen / Esc](#)[Printer-friendly Version](#)[Interactive Discussion](#)

## Local and regional scale measurements of CH<sub>4</sub>, δ<sup>13</sup>CH<sub>4</sub>, and C<sub>2</sub>H<sub>6</sub> in the Uintah Basin

C. W. Rella et al.

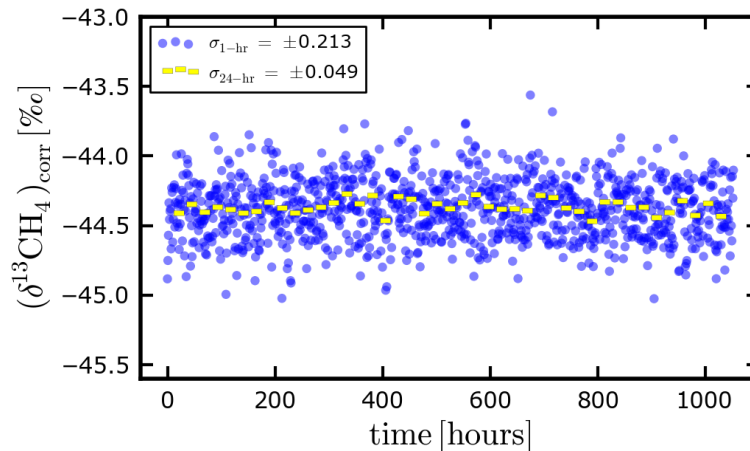


**Figure 9.** Hourly measurements of  $\delta^{13}\text{CH}_4$ , after correction. The SD of the hourly measurements (blue circles) and the daily measurements (yellow bars) are shown in the figure legend.

[Title Page](#)[Abstract](#)[Introduction](#)[Conclusions](#)[References](#)[Tables](#)[Figures](#)[◀](#)[▶](#)[◀](#)[▶](#)[Back](#)[Close](#)[Full Screen / Esc](#)[Printer-friendly Version](#)[Interactive Discussion](#)

## Local and regional scale measurements of CH<sub>4</sub>, δ<sup>13</sup>CH<sub>4</sub>, and C<sub>2</sub>H<sub>6</sub> in the Uintah Basin

C. W. Rella et al.

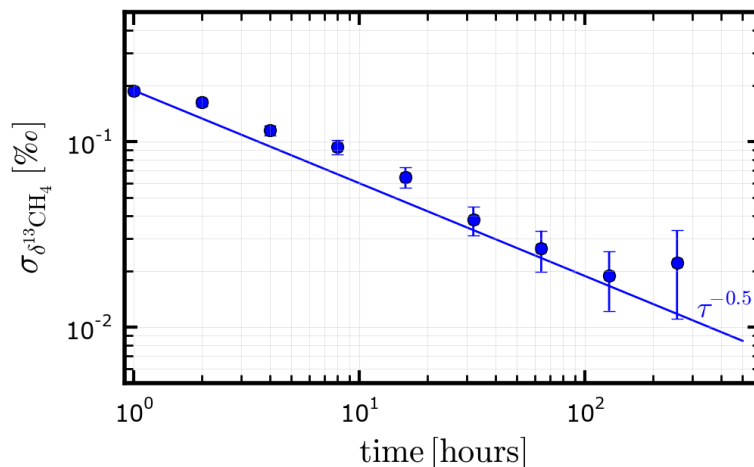


**Figure 10.** Allan standard deviation of  $\delta^{13}\text{CH}_4$  after correction, using the data in Fig. 16. The  $\tau^{-1/2}$  line is shown for reference, indicating that the noise is nearly random, at least over 100 h. There is a perceptible increase in the Allan standard deviation at about 12 h, which may indicate a moderate dependence of  $\delta^{13}\text{CH}_4$  on the diurnal cycle. The error bars are estimated based upon the averaging time and the time duration of the data set.

[Title Page](#)[Abstract](#)[Introduction](#)[Conclusions](#)[References](#)[Tables](#)[Figures](#)[◀](#)[▶](#)[◀](#)[▶](#)[Back](#)[Close](#)[Full Screen / Esc](#)[Printer-friendly Version](#)[Interactive Discussion](#)

## Local and regional scale measurements of CH<sub>4</sub>, δ<sup>13</sup>CH<sub>4</sub>, and C<sub>2</sub>H<sub>6</sub> in the Uintah Basin

C. W. Rella et al.

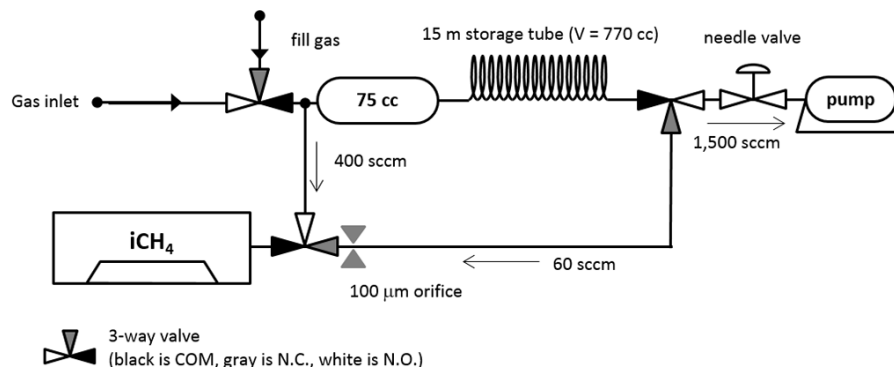


**Figure 11.** Apparatus for measuring the isotope ratio and ethane-to-methane ratio of single plumes in the mobile lab. For survey mode, all 3-way valves are in “normally-open” (N.O.) position (white), and the instrument measures the real time signal at the input to the 770 cc storage tube. The flow through the tube is set by the pump and needle valve. When a plume is detected at the instrument, the 3-way valves are switched to “normally-closed” (N.C.) position (gray) and the instrument slowly re-analyzes the gas stored in the long tube.

Title Page

Abstract

Introduction

Conclusions

References

Tables

Figures

◀

▶

◀

▶

Back

Close

Full Screen / Esc

Printer-friendly Version

Interactive Discussion

## Local and regional scale measurements of CH<sub>4</sub>, δ<sup>13</sup>CH<sub>4</sub>, and C<sub>2</sub>H<sub>6</sub> in the Uintah Basin

C. W. Rella et al.

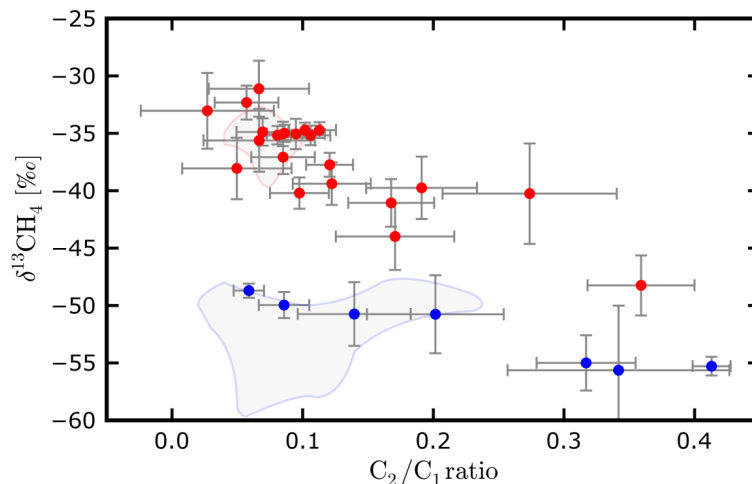


**Figure 12.**  $\delta^{13}\text{CH}_4$  and ethane-to-methane ratios for plumes from 21 natural gas wells (red) and 7 oil wells (blue) in the Uintah basin. All of the natural gas measurements were of plumes in the Natural Buttes field in the basin; the oil well measurements were mostly in the Monument Butte field. The natural gas signatures are consistent with previous observations of production gases in the Uintah Basin (Rice et al., 1992), and follow trends observed in other formations for gas associated with oil production and non-associated thermogenic natural gas of various levels of maturation. The red- and blue-outlined gray areas represent distinct populations of wells in the Uintah as described in Rice et al. (1992), for which it has been assumed (for simplicity) that the contribution of propane and heavier alkanes is zero. The centroids of the distribution of gas well signatures is  $-37.18 \pm 3.9\text{‰}$  and  $0.118 \pm 0.075$  for  $\delta^{13}\text{CH}_4$  and ethane-to-methane ratios, respectively, and for oil is  $-52.31 \pm 2.7\text{‰}$  and  $0.223 \pm 0.13$ .

Title Page

Abstract

Introduction

Conclusions

References

Tables

Figures

◀

▶

◀

▶

Back

Close

Full Screen / Esc

Printer-friendly Version

Interactive Discussion

## Local and regional scale measurements of $\text{CH}_4$ , $\delta^{13}\text{CH}_4$ , and $\text{C}_2\text{H}_6$ in the Uintah Basin

C. W. Rella et al.

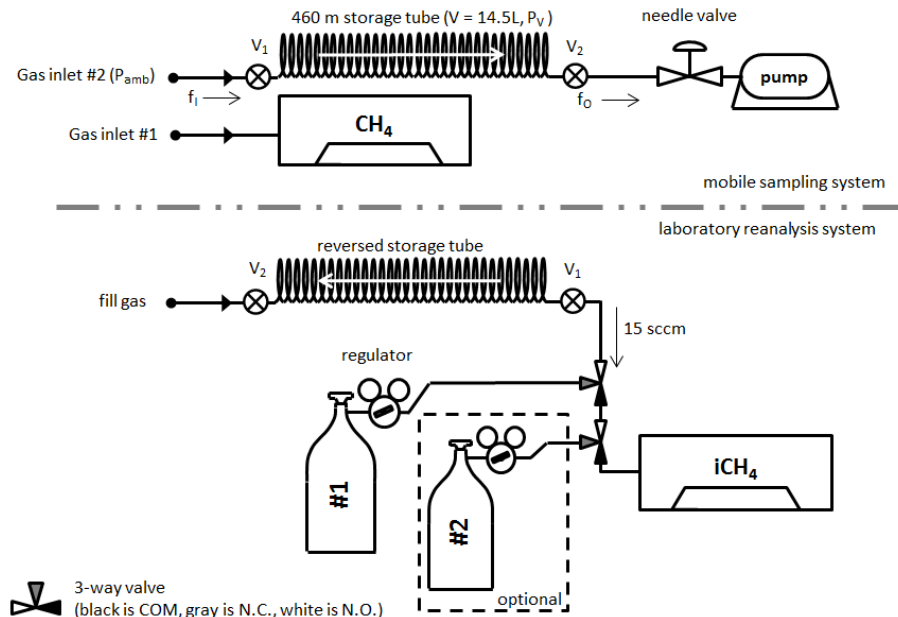


**Figure 13.** Apparatus for making regional isotope and ethane ratio measurements. The top schematic shows the mobile sampling system. The flow through the long storage tube is set by the pump and needle valve. The two manual valves ( $V_1$  and  $V_2$ ) are in the open position during the measurements, and closed when the survey is complete. An optional flow meter can be inserted in the line upstream of the storage tube to verify the actual flow into the instrument. An instrument in the vehicle measures the local ambient concentration on a separate inlet. The storage tube is transported to the laboratory (lower schematic), where the gas stored in the long tube is reanalyzed slowly (with the flow reversed, so the last gas in is the first out). The reanalysis is periodically interrupted to run one or more calibration standard. A gas drying system can be introduced downstream of the storage tube in the laboratory to reduce the possible effect of water vapor on the measurements, but this was not done in the results reported here. A fill gas other than ambient air can be used to denote the end of the sample.

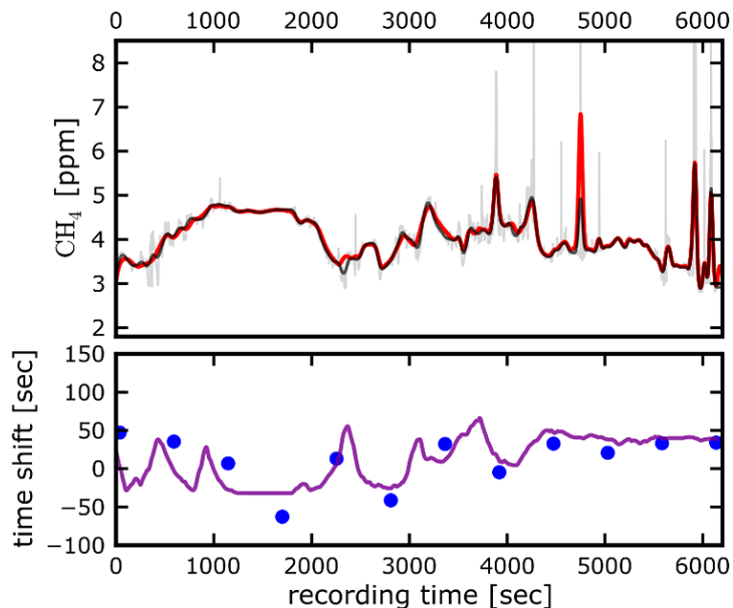


**Figure 14.** Top panel: (light gray) methane signal recorded in the vehicle over about 1.6 h. Some plumes are as large as 30 ppm. (dark gray) Methane signal recorded in the vehicle, after applying the smoothing function derived from gas diffusion in the storage tube. (red) Methane signal obtained during re-analysis of the gas stored in the tube over about 24 h of analysis time. The time axis of the reanalyzed signal has been adjusted according to the ratio of the flows during recording and reanalysis. To account for flow differences in different parts of the drive, the replay time axis is compressed or expanded using a cubic spline function with 15 knots across the time axis (every 300 s), optimizing the time mismatch between the recorded methane signal and the reanalyzed signal. These time shifts are shown in the bottom panel (blue points) (where a positive value indicates that the reanalysis time should be shifted later, indicative of a reduced flow into the tube). The purple line in the bottom panel is the time shift predicted by the inlet flow model for this drive described in the Supplement – the only free parameter was an overall offset to the modeled time shift.

**Local and regional scale measurements of CH<sub>4</sub>, δ<sup>13</sup>CH<sub>4</sub>, and C<sub>2</sub>H<sub>6</sub> in the Uintah Basin**

C. W. Rella et al.

Title Page	
Abstract	Introduction
Conclusions	References
Tables	Figures
◀	▶
◀	▶
Back	Close
Full Screen / Esc	
Printer-friendly Version	
Interactive Discussion	





## Local and regional scale measurements of CH<sub>4</sub>, δ<sup>13</sup>CH<sub>4</sub>, and C<sub>2</sub>H<sub>6</sub> in the Uintah Basin

C. W. Rella et al.

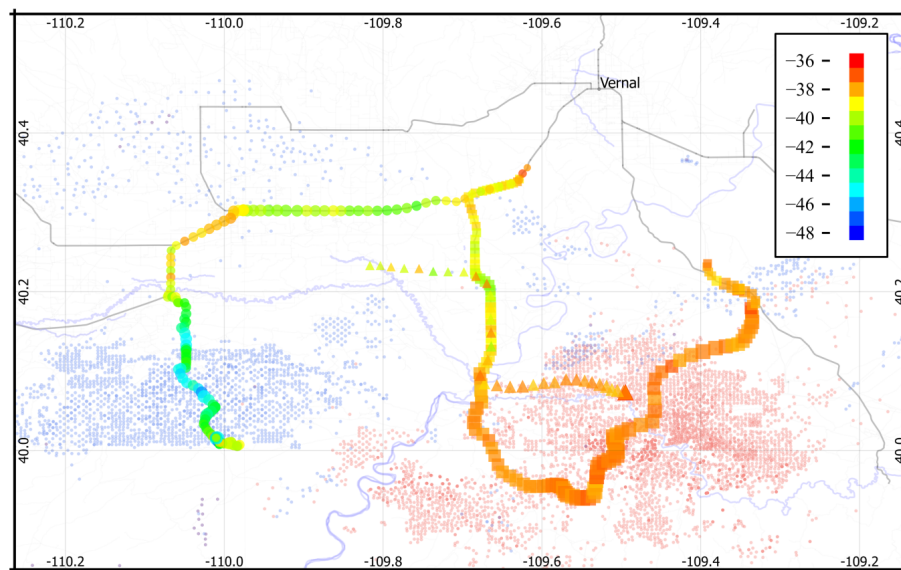


**Figure 15.** Map of the Uintah basin, showing the locations of oil wells (blue) and gas wells (red). In addition, the gas measurements obtained from the three regional drives are plotted, where the area of the symbol is proportional to the gas concentration above background levels, and the color given by the isotope ratio, with heavy ratios in red and light ratios in blue. Symbols correspond to the date of the measurement (circles: 1 February 2013; squares: 3 February 2013; triangles: 9 February 2013). Concentrations are highest in the primary gas production area in the southeast, and the observed isotope ratio is heavy. Isotope ratios in the oil producing areas are lightest, and the concentrations are lower. The concentrations have been scaled so that common segments of the drives have the same average concentration (see text for details). Map image generated by Quantum GIS (Quantum, 2013); road and waterways data© OpenStreetMap contributors.

Title Page

Abstract

Introduction

Conclusions

References

Tables

Figures

◀

▶

◀

▶

Back

Close

Full Screen / Esc

Printer-friendly Version

Interactive Discussion

## Local and regional scale measurements of CH<sub>4</sub>, δ<sup>13</sup>CH<sub>4</sub>, and C<sub>2</sub>H<sub>6</sub> in the Uintah Basin

C. W. Rella et al.

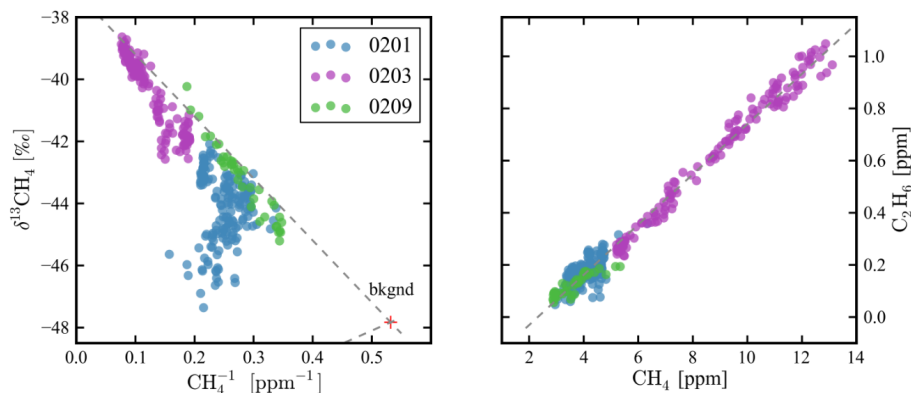


**Figure 16.** (Left panel) Keeling plot of  $\delta^{13}\text{CH}_4$  vs.  $(\text{CH}_4)^{-1}$  for the three drives on 1 February, 3 February, and 9 February in 2013. The point labeled “bkgnd” is the measurement of Niwot Ridge, Colorado air by NOAA in February 2012:  $\text{CH}_4 = 1.880$  ppm and  $\delta^{13}\text{CH}_4 = -47.83$ ‰ (Dlugokencky et al., 2014). The top gray line indicates a source of gas with a  $-37.2$ ‰ isotope ratio (the centroid of the individual gas sources in Fig. 12), and the bottom gray line indicates a source of  $-52.3$ ‰ (the centroid of the individual oil sources in Fig. 12). Clearly the majority of the observed isotope ratios are dominated by gas sources. (Right panel) Plot of ethane vs. methane for the same three drives. The gray dashed line follows an ethane-to-methane ratio of 0.096.

Title Page

Abstract

Introduction

Conclusions

References

Tables

Figures

◀

▶

◀

▶

Back

Close

Full Screen / Esc

Printer-friendly Version

Interactive Discussion

